

NASA/TM-20230006779



Plug20 Test Report: Particle Image Velocimetry (PIV) Measurements

*James Bridges and Mark P. Wernet
Glenn Research Center, Cleveland, Ohio*

*Puja Upadhyay and Heath H. Reising
HX5, LLC, Brook Park, Ohio*

NASA STI Program . . . in Profile

Since its founding, NASA has been dedicated to the advancement of aeronautics and space science. The NASA Scientific and Technical Information (STI) Program plays a key part in helping NASA maintain this important role.

The NASA STI Program operates under the auspices of the Agency Chief Information Officer. It collects, organizes, provides for archiving, and disseminates NASA's STI. The NASA STI Program provides access to the NASA Technical Report Server—Registered (NTRS Reg) and NASA Technical Report Server—Public (NTRS) thus providing one of the largest collections of aeronautical and space science STI in the world. Results are published in both non-NASA channels and by NASA in the NASA STI Report Series, which includes the following report types:

- TECHNICAL PUBLICATION. Reports of completed research or a major significant phase of research that present the results of NASA programs and include extensive data or theoretical analysis. Includes compilations of significant scientific and technical data and information deemed to be of continuing reference value. NASA counter-part of peer-reviewed formal professional papers, but has less stringent limitations on manuscript length and extent of graphic presentations.
- TECHNICAL MEMORANDUM. Scientific and technical findings that are preliminary or of specialized interest, e.g., “quick-release” reports, working papers, and bibliographies that contain minimal annotation. Does not contain extensive analysis.
- CONTRACTOR REPORT. Scientific and technical findings by NASA-sponsored contractors and grantees.
- CONFERENCE PUBLICATION. Collected papers from scientific and technical conferences, symposia, seminars, or other meetings sponsored or co-sponsored by NASA.
- SPECIAL PUBLICATION. Scientific, technical, or historical information from NASA programs, projects, and missions, often concerned with subjects having substantial public interest.
- TECHNICAL TRANSLATION. English-language translations of foreign scientific and technical material pertinent to NASA's mission.

For more information about the NASA STI program, see the following:

- Access the NASA STI program home page at <http://www.sti.nasa.gov>
- E-mail your question to help@sti.nasa.gov
- Fax your question to the NASA STI Information Desk at 757-864-6500
- Telephone the NASA STI Information Desk at 757-864-9658
- Write to:
NASA STI Program
Mail Stop 148
NASA Langley Research Center
Hampton, VA 23681-2199

NASA/TM-20230006779



Plug20 Test Report: Particle Image Velocimetry (PIV) Measurements

*James Bridges and Mark P. Wernet
Glenn Research Center, Cleveland, Ohio*

*Puja Upadhyay and Heath H. Reising
HX5, LLC, Brook Park, Ohio*

National Aeronautics and
Space Administration

Glenn Research Center
Cleveland, Ohio 44135

September 2023

Acknowledgments

The Plug20 test was supported by the NASA Commercial Supersonic Technology project, under the Advanced Air Vehicle Program.

This work was sponsored by the Advanced Air Vehicle Program
at the NASA Glenn Research Center

Trade names and trademarks are used in this report for identification
only. Their usage does not constitute an official endorsement,
either expressed or implied, by the National Aeronautics and
Space Administration.

Level of Review: This material has been technically reviewed by technical management.

Plug20 Test Report: Particle Image Velocimetry (PIV) Measurements

James Bridges and Mark P. Wernet
National Aeronautics and Space Administration
Glenn Research Center
Cleveland, Ohio 44135

Puja Upadhyay* and Heath H. Reising
HX5, LLC
Brook Park, Ohio 44142

Abstract

This report provides turbulent flow statistics made using particle image velocimetry (PIV) for several internally mixed exhaust systems with external plugs (Plug20 designs). The tests were conducted at the NASA Glenn Research Center’s Aero-Acoustic Propulsion Laboratory (AAPL) in May and June 2022. The corresponding acoustic data for the configurations and flows presented in this report can be found in an earlier Technical Memorandum, NASA/TM-20210010291, “Plug20 Test Report.”

The Plug20 nozzle family was designed to represent commercial supersonic vehicles in the 2025 to 2035 timeframe with a bypass ratio around 4, having an internal mixer, with and without an external plug to improve nacelle boattail drag and shock. The flow conditions measured represent engine cycles for commercial supersonic aircraft at takeoff, having pressure ratios of 2.0 and heated fan and core streams, measured both with and without a flight stream surrounding the plume. A few unheated flow conditions were also tested to tie results to other baseline test results. The PIV measurements in both streamwise and cross-stream planes are described, along with brief analysis to visually catalog the contents and confirm their validity. In this analysis, the streamwise PIV is found to match benchmark datasets within its experimental error. However, the cross-stream turbulent quantities measured by two systems do not match each other or the streamwise measurements in amplitude—caution is required when using the cross-stream data.

Data acquired and included in this report are (1) velocity statistics of the plumes in both a streamwise and several cross-stream planes, and (2) the hot nozzle geometry. Tabular forms of the data and computer-aided design (CAD) files of the hot geometry are presented as supplemental files described in Appendix A (TM-20230006779SUPPL1.zip) and Appendix B (TM-20230006779SUPPL2.zip).

Nomenclature

AAPL	Aero-Acoustic Propulsion Laboratory
CAD	computer-aided design
CFD	computational fluid dynamics
D_{jet}	nozzle exit diameter
FOV	field of view
HFJER	High Flow Jet Exit Rig

*Currently with NASA Glenn Research Center.

LogLUT	logarithmic look-up table
Ma	Mach number, ideally expanded, based on ambient speed of sound
M_f	Mach number of freejet (flight stream)
M, M_{id}	Mach number, ideally expanded, based on speed of sound in flowing gas
NATR	Nozzle Aeroacoustic Test Rig
NPR	nozzle pressure ratio, jet total pressure/ambient pressure
NTR	nozzle temperature ratio, jet total temperature/ambient temperature
PIV	particle image velocimetry
RANS	Reynolds-averaged Navier–Stokes
SPOF	symmetric phase-only filtering
U_{jet}	jet exit velocity, fully expanded

Subscripts

b	bypass
c	core

Introduction

The engine jet plume is the dominant noise source of commercial supersonic aircraft proposed for entry into service between 2025 and 2035. Due to cruise performance, nozzles with internal mixing of core and bypass streams with large external plugs are being considered for these aircraft. Empirical noise prediction methods generally do not account for the presence of internal mixers or an external plug, and have no ability to account for differences in internal mixer design. Previously, tests have been made of exhaust systems with internal mixers and published results (Refs. 1 to 3) show the difficulty in creating such models. More advanced methods, such as Reynolds-averaged Navier–Stokes-based computational fluid dynamics (RANS-based CFD) with acoustic analogy noise codes, may be adequate, but they do not account for the presence of the plug and cannot predict the propagation of noise generated internal to the nozzle. Furthermore, external plug nozzles have shocks from the curvature of the flow over the crown of the plug and no method exists to predict this noise source. It is also anticipated that the close proximity of the nozzle shear layer with an elongated plug may change the coupling of the turbulence with the acoustic field. Indeed, some work (Ref. 4) has shown that a properly shaped plug may even produce noise reduction.

As data for plug nozzles such as these are scarce, a baseline test was needed to determine the accuracy of the various noise prediction methods. This test was intended to also determine the sensitivity of the noise to internal mixer design, plug length, and shape. In 2019, a series of nozzles with interchangeable mixers and plugs were designed and fabricated based on RANS predictions of their impacts on the jet plume and anticipated change in far-field noise. Acoustic and schlieren measurements were initially made and documented (Ref. 5). Analysis of these results (Ref. 6) guided the design of the subsequent flow measurements being reported here. It also dictated that additional far-field noise measurements be made, which correspond to some of the configurations measured using particle image velocimetry (PIV) and included in this report.

Facility

The test was conducted in the NASA Glenn Research Center's Aero-Acoustic Propulsion Laboratory (AAPL). The AAPL is a 65-ft-radius anechoic geodesic hemispherical dome.

The test nozzles were placed on a jet engine simulator, itself centered in the Nozzle Aeroacoustic Test Rig (NATR) contained in the AAPL. The NATR provides the flight stream for the jet rig. The NATR ductwork consisted of an annular ejector system connected to a plenum followed by the transition section, which is a long-radius, low-beta venturi nozzle. This flow exhausts through a 53-in.-diameter nozzle to form a freejet to simulate the effects of flight on the test article. This arrangement produced the Mach 0.3 flight stream used in some test points.

A turbofan engine simulator, the High Flow Jet Exit Rig (HFJER), was located at the downstream end of the NATR (Figure 1). Compressed air from centralized compressors was delivered to the test article through a system of manifolds, heaters, flow-measuring venturis, control valves, and flow conditioners. All air streams were preheated using a mixed flow heat exchanger before being split into two streams, independently metered and pressure controlled, and directed to co-annular settling chambers in the rig. The innermost air stream was further heated using a natural gas combustor up to 1,350 °F (1,005 K).

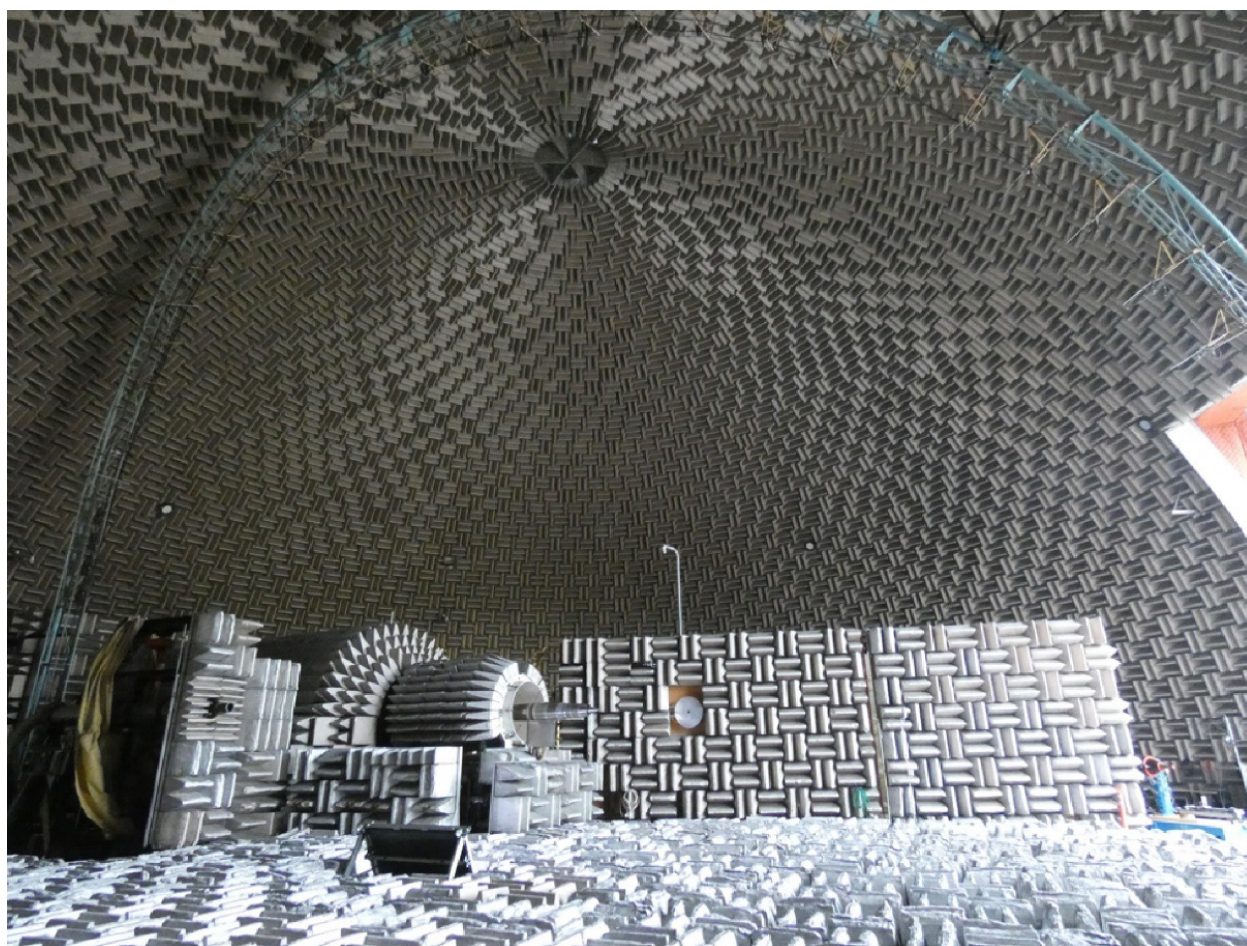


Figure 1.—Test venue, with HFJER located at exit of NATR, located within anechoically treated AAPL.

The rig was instrumented to record total temperature, total pressure, and static pressure at a charging station on all streams. In addition, mass flowrates were recorded using venturi meters. Ambient conditions were recorded simultaneously with the acoustic and flow measurements. Ambient pressure was recorded in a sheltered location within the dome.

Model Hardware Configurations

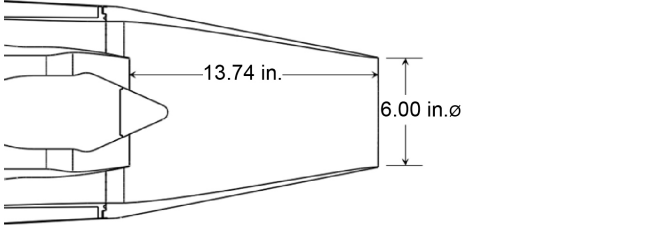
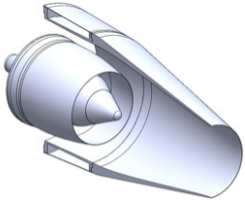
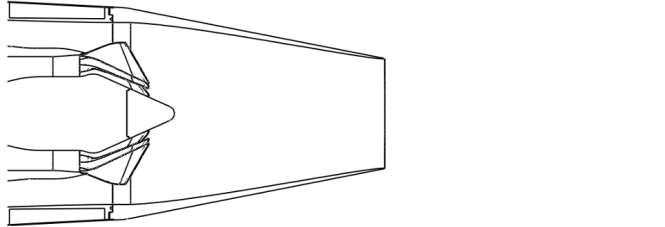
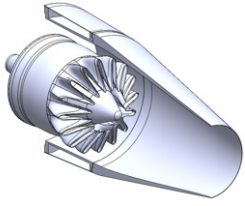
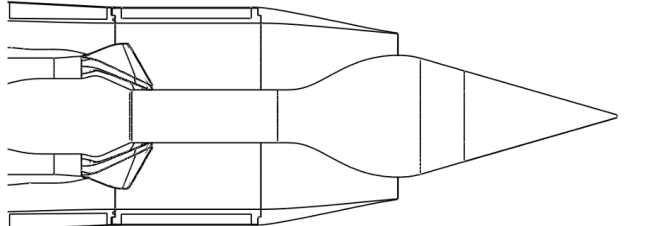
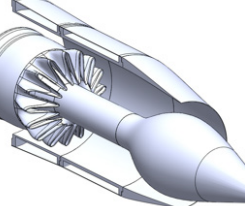
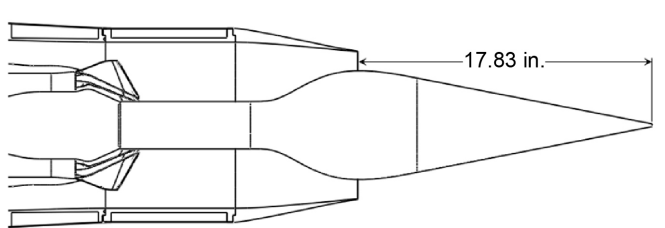
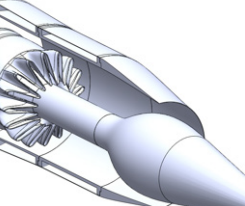
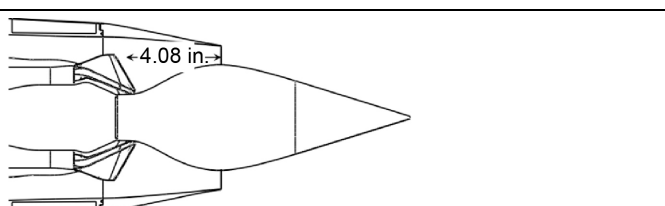
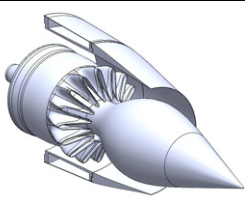
Model configurations are comprised of a combination of plug, internal mixer, and nozzle. Configurations were first grouped as internal versus external plugs. The internal plug configuration used nozzle *A*, with a choice of interchangeable mixers (*mix0*, *mix5*). One internal plug shape, a round-nose cone labeled *pInt*, completed the internal plug configurations.

The external plug configurations used nozzle *D*, and in PIV testing one of two plugs (*p2069*, *p2079*) that were used interchangeably with the two mixers. In addition, spacers in the plug stem and nozzle duct allow a 7.9-in. (0.2-m) change between the mixer and the nozzle exit plane. Thus, the external nozzle designation was *DS* (short, without extensions) or *DL* (long, with extensions). Table I contains visual representations and key dimensions of the five nozzle configurations as designed.

One benefit of using PIV instrumentation is the high-definition cameras that can image the test hardware and allow measurement of true model geometry. For exhaust systems, the primary change in geometry is relative length of the inner and outer nozzles as they are heated differently by the hot core and colder bypass streams. The external plug, being anchored upstream in the core stream, will also have different thermal growth than the nozzles. It was also found that the jet rig itself had a downward angle of 0.46° relative to true horizontal (to which the traverse and PIV system were referenced). In the PIV dataset being released, the coordinate system (including mean velocity components) has been adjusted to align with the rig axis as determined by the normal to the nozzle flange. No interpolation of the PIV data was made, which explains why the axial dimensions are not constant on a constant radial index.

Subsequent to the test, PIV images of the nozzle system were analyzed photogrammetrically to find the true “hot” shapes of the models during testing (Figure 2). One unexpected variation with temperature was a vertical droop in the plug, which depended upon plug length and core temperature. Using this analysis with the model at setpoint 1200 (as defined in the “Flow Conditions” section), hot shape geometry computer-aided design (CAD) models were produced to reflect the true geometry as tested for all external plug configurations, incorporating axial growth of the mixer/splitter and the added vertical asymmetry of the external plug. Hot shapes for the internal configurations only involve the axial growth of the internal parts as determined from the axial changes in external plug geometry. For each configuration, there are two geometries given in the appendixes, a cold and hot version to be used in validation work. In all cases, the nozzle exit plane is taken to be the origin of the coordinate system. These configurations should also be used in validation work attempting to match acoustic results from previous testing of the Plug20 model system. Flow deviations from symmetry about the new centerline are due to nozzle asymmetries and should be reproducible if the hot shape nozzle geometry is used.

TABLE I.—NOZZLE CONFIGURATIONS TO BE TESTED IN PLUG20 PIV

<p><i>Am0pInt</i></p>		
<p><i>Am5pInt</i></p>		
<p><i>DLm5p2069</i></p>		
<p><i>DLm5p2079</i></p>		
<p><i>DSm5p2069</i></p>		

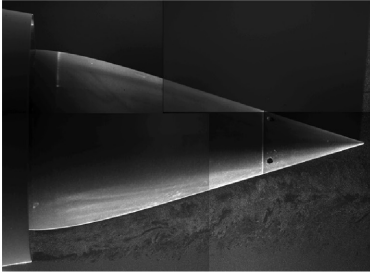
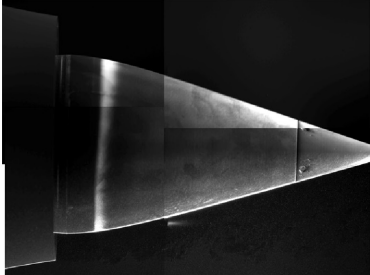
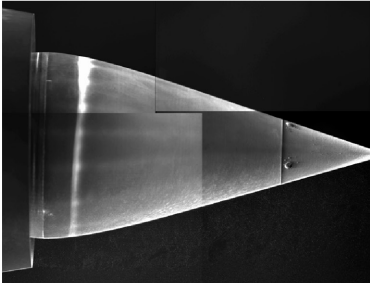
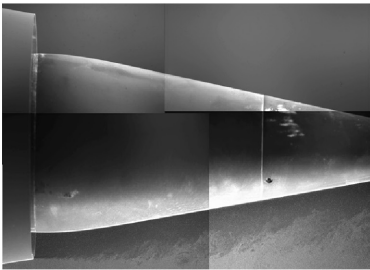
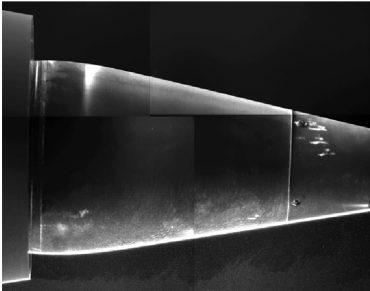
Configuration	Imagery	Plug deviations
<i>DLm5p2069</i> cold		Offset = 2.6 mm Angle = -0.26°
<i>DLm5p2069</i> hot		Offset = 11.3 mm Angle = -1.24°
<i>DSm5p2069</i> hot		Offset = 11.2 mm Angle = -1.18°
<i>DLm5p2079</i> cold		Offset = 3.2 mm Angle = -0.83°
<i>DLm5p2079</i> hot		Offset = 11.0 mm Angle = -1.71°

Figure 2.—Hot shape deviations of external plugs, determined from photogrammetry. Vertical offsets measured at nozzle exit.

Flow Conditions

The flow conditions are meant to mimic a potential two-stream engine for commercial supersonic aircraft. The flows studied here are a subset of those previously studied (Ref. 5). The flow conditions used in PIV testing are given in Table II. The setpoints were held constant to within a total error in NPR , NTR_c , NTR_b , and M_f of 0.5 percent.

Setpoint 70 was intended to tie this dataset to previous jet databases, this unheated $Ma = 0.90$ flow having been acquired in many previous single-stream jet tests. Setpoints 71, 73, and 75 were intended to capture the impact of a flight stream on the setpoint 70 jet flow, including the boundary layer external to the nozzle.

Setpoint 1200 was a flow condition from a previous concept aircraft (Ref. 7) at $NPR = 2.000$, and represents a challenging condition of slightly underexpanded flow. Setpoint 1203 is the same jet flow in a $M_f = 0.3$ flight stream.

Setpoints 3200 and 4200 are related in that they both have the same fully mixed jet condition. In both flows, the $NPR = 2.000$ on both streams, but setpoint 4200 has both streams running at the highest temperature that the fan stream can reach. Setpoint 3200 then is set by the fan stream at its coldest (unheated) and the core stream set at the temperature ratio that gives the fully mixed temperature of setpoint 4200. Not all conditions, or setpoints, were tested for all nozzles. (See Table IV for the actual test point matrix.)

Instrumentation

The engine simulator was instrumented to record total temperature, total pressure, and static pressure at a charging station (representing engine station 7 on an engine) on all streams. In addition, mass flowrates were recorded using venturi meters. Ambient conditions in the dome were recorded simultaneously with the flow measurements.

The jet flow streams were seeded using a pH-stabilized dispersion of $\sim 0.4\text{-}\mu\text{m}$ -diameter alumina particles in ethanol (Ref. 8). The stabilized dispersion of alumina was introduced into the flow well upstream of the model by atomizing the dispersion in each of the three engine streams. The ambient flow from the facility freejet was seeded using a propylene glycol fog of $\sim 0.7\text{-}\mu\text{m}$ -diameter-sized particles. Multiple Roscoe foggers, models 3000 and 6000, situated in the freejet ejector inlet room of NATR, produced the fog that seeded the ambient, or flight, air. For setpoints with $M_f = 0$, two 2-ft-diameter ventilation fans provided the slight ambient flow at a nominal speed of $M_f = 0.01$. At these conditions, it was difficult to maintain consistently uniform seeding in the ambient, leading to a low number of valid measurements in these regions.

TABLE II.—FLOW CONDITIONS MATRIX

Setpoint	NPR	NTR_c	NTR_b	M_f	U_{jets} , m/s
70	1.856	1	1	0	308
71	1.856	1	1	0.1	308
73	1.856	1	1	0.2	308
75	1.856	1	1	0.3	308
1203	2.000	3.25	1.2	0.3	588
1200	2.000	3.25	1.2	0	588
3200	2.000	2.75	1	0	540
4200	2.000	1.31	1.31	0	372

PIV measurements were made in two configurations: two-component velocity measurements in a streamwise plane including the jet centerline, and three-component measurements in cross-stream planes. All optical equipment was mounted on a large traversing frame, which moved parallel to the jet axis (Figure 3).

Streamwise PIV (PIVs). The two-component streamwise plane system was implemented with a vertical light sheet coming from below the jet, aligned with the outward lobes of the mixer for configurations containing the *m5* mixer. For this reason, on configurations with an external plug, no data were obtained above the plug. To avoid reflection off the round nozzle into the cameras, the laser sheet was offset by 1 mm to the side away from the cameras and the nozzle painted flat black.

For this test, we required a large field of view (FOV) to cover the transverse extent of the plume, which was accomplished using a 2×2 array of Princeton Instruments ES11000 cameras equipped with 180-mm focal length lenses and 8-mm extension tubes (Figure 4). Each camera had a FOV of 7.6×11.4 in. (193×290 mm). The combined 2×2 camera overlap yielded a 13.5×21.2-in. (344×539-mm) FOV. The PIV image data and laser timing were controlled via an in-house package called PIVACQ, which displayed the acquired camera images in a 2×2 display on the data acquisition computer.

To measure the jet plume, the optical equipment was traversed axially to overlapping stations and sampled independently at each station. A black-velvet-lined shadow box was placed on a shelf opposite the cameras to provide a dark background in the PIV images and prevent ambient daylight from illuminating the background. The axial stations were measured at 12-in. (304.8-mm) intervals, yielding 1.63-in. (41.3-mm) overlap between axial traverse stations. Measurements were thus made for seven stations, covering a total measurement field of 85.2 in. (2.16 m), limited by the axial extent of the traverse to just over 14 nozzle diameters.

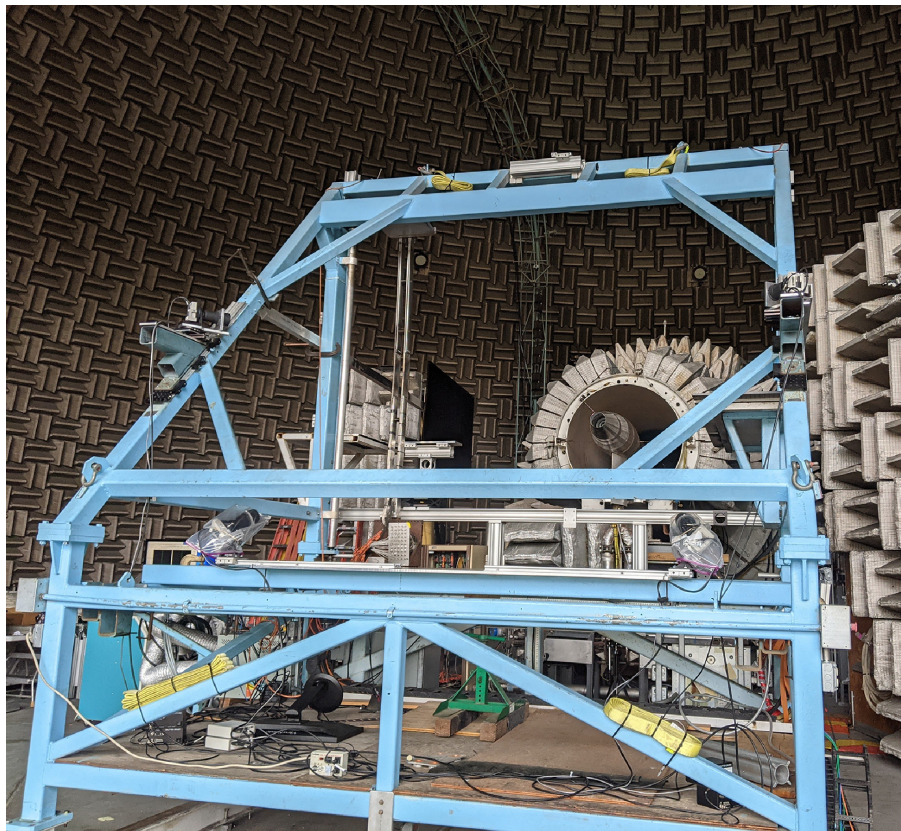


Figure 3.—Traverse to move optical components established via NATR.

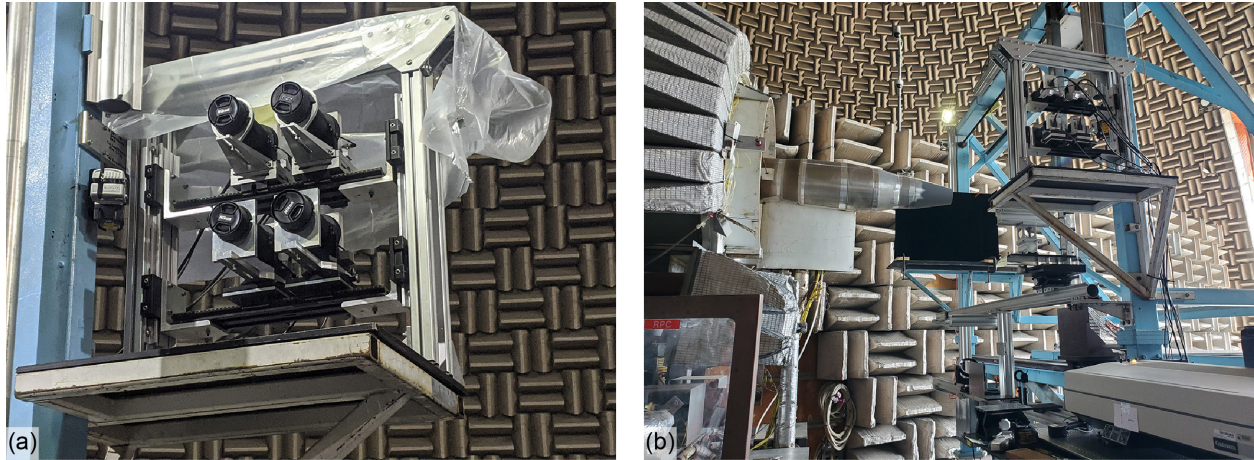


Figure 4.—Streamwise PIV setup. (a) 2x2 camera array. (b) With black velvet backdrop.

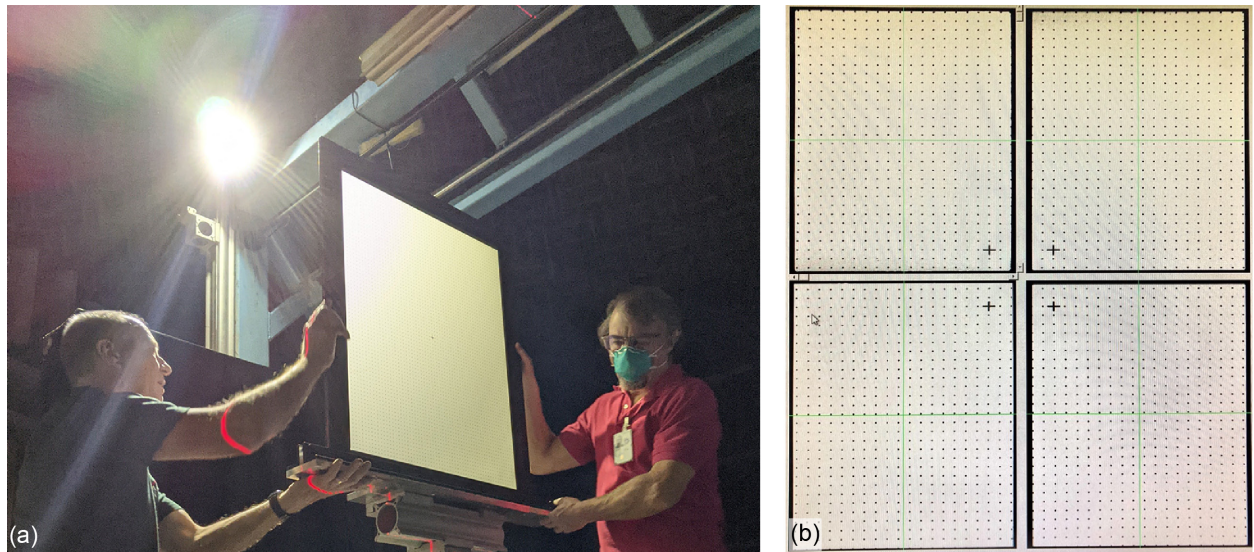


Figure 5.—Large, high-precision targets used for camera calibration. (a) Installation of streamwise calibration target. Note two grid row overlap (10-mm grid on target). (b) Sample PIVACQ screen capture illustrating 2x2 camera calibration.

In daily setup for streamwise PIV, the jet axis was established with a line on the floor, established from the projection of a light sheet normal to the rig flange, and confirmed to hit the center of the nozzle. An autoleveling laser sheet was established that was parallel to the established centerline, offset horizontally away from the cameras by 1 mm. The PIV laser was aligned with this reference light and the cameras were focused on the PIV laser sheet by imaging room dust particles. The four cameras were then calibrated using a large, high-precision target (Figure 5), again aligned with the reference light sheet. A center fiducial mark that was imaged for all cameras in the 2x2 configuration was used in establishing the relative location of each camera's FOV.

PIV images were converted to velocity vector maps using PIVPROC in-house software. The PIV image data were processed using 64x64 pixel subregions on a 32x32 pixel grid for the first pass, then using six passes (simulated annealing) at 32x32 pixel resolution on a 16x16 grid, and two final passes using subregion distortion processing with 32x32 pixel subregions on a 16x16 pixel grid. The resulting processed velocity grid resolution was 0.047 in. (1.2 mm).

Cross-stream PIV (PIVx) While the nozzle is nominally axisymmetric, the flow was not because of the internal lobed mixer, which will not completely mix the flows by the nozzle exit. Measuring the degree of nonaxisymmetry required cross-stream PIV. This measurement was very difficult for two reasons: optical access and the illuminated background.

The description of the optical setup starts with considerations of optical access. To obtain stereo PIV information at a point, the laser and both cameras must fall on that point. For acquisition planes upstream of the nozzle and/or plug tip, the model blocked the camera views and the laser light sheet. With an external plug blocking the laser sheet from below, all regions above the nozzle and/or plug are lost. With standard stereo PIV, the cameras are 180° apart azimuthally around the jet axis, and roughly 45° in the polar angle from the downstream axis of the jet. (They both lie in the horizontal plane.) The external plug, therefore, blocks each camera from seeing the light sheet on the opposite side of the plug. So, no data can be obtained from the flow on the sides of the plug. This leaves a small segment below the plug where particles can be illuminated by the light sheet and imaged by both cameras, as shown in Figure 6. Cross-stream PIV data acquired with the standard optical setup described previously are referred to as “PIVxa.”

A novel approach to improve on the amount of the plane that could be measured is shown in Figure 7. The cameras were moved around the jet axis such that they each see more of the other’s nonoccluded FOV around the plug. Simply placing the cameras at these locations would have required a double Scheimpflug angle to be used (to make the image be in focus across the optical sensor requires that the focusing lens be set at an intermediate angle to the light sheet and the optical sensor). However, a single Scheimpflug mount could be used if the cameras and mounts were also rotated around the jet axis, keeping the same angle between optical sensor and light sheet. The cameras each being rotated by 45° downward around the jet axis, they were now 90° apart azimuthally, and still were positioned at a polar angle 45° from the downstream axis of the jet. Processing the stereo images required special treatment as, instead of the two cameras having a common horizontal displacement in their images, now the one camera’s horizontal component of displacement is the other’s vertical component. Cross-stream PIV data acquired with this nonstandard optical setup are referred to as “PIVxb.”

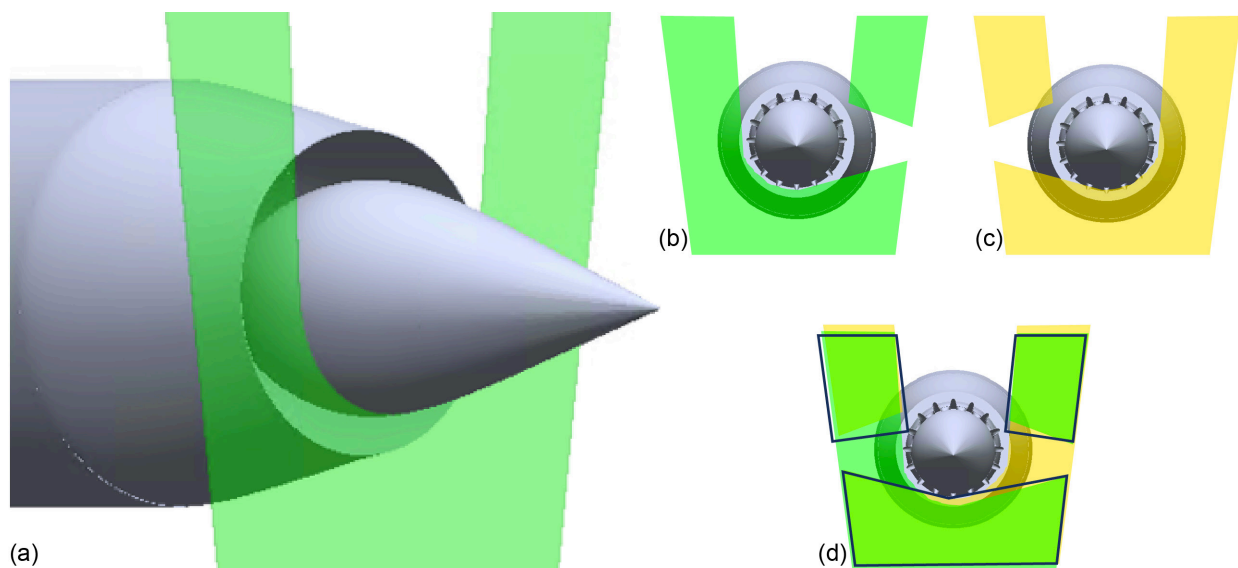


Figure 6.—Standard stereo PIV configuration (PIVxa). Regions of common optical access on cross-stream planes along external plug. (a) Laser sheet blocked by plug. (b) Light sheet illuminated lower left camera view. (c) Light sheet illuminated right camera view. (d) View in common .

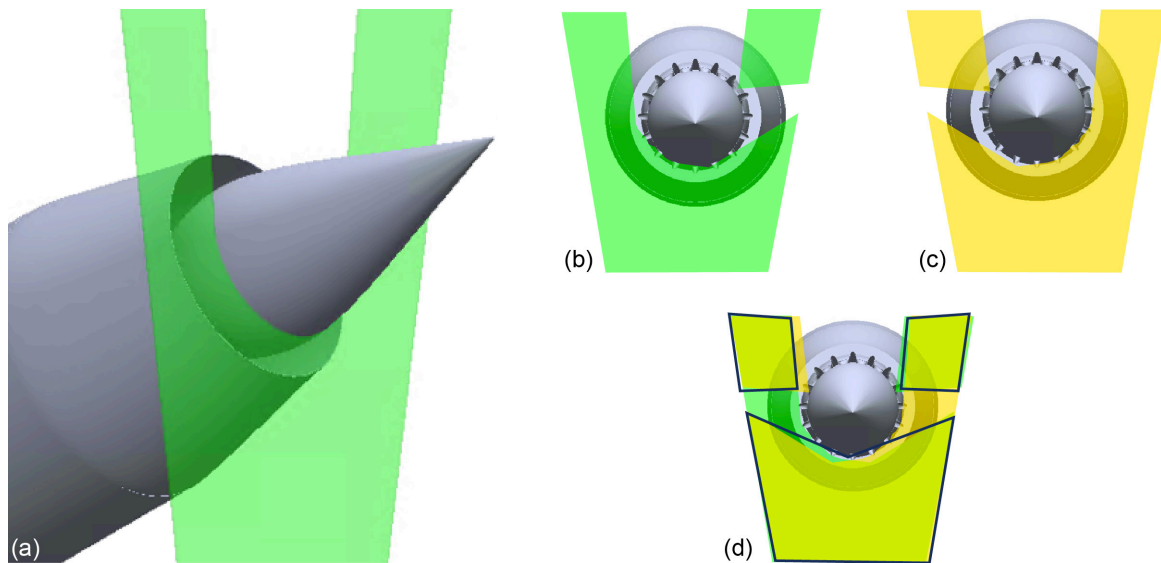


Figure 7.—Nonstandard stereo PIV configuration (PIVxb). Regions of common optical access providing extended flow domain of measurement along external plug. (a) View from 45° below model. (b) Light sheet illuminated left camera view. (c) Light sheet illuminated right camera view. (d) Common area from both camera views.

A 10-mm vellum grid target was used for the cross-stream calibrations, at nine planes with 0.5-mm spacings between planes. Insight software (TSI Incorporated) was used to create the image mapping from the vellum target to the camera image planes for the standard optical setup. Processing of the images using the Insight-generated calibration was performed using in-house software.

The TSI calibration software could not accommodate the nonstandard configuration and DaVis image acquisition and processing software (LaVision, Inc.) was used instead. To properly orient the DaVis-processed data, the DaVis target was rotated in the plane of the laser sheet by 45°, so that the calibration targets filled the lower camera pair FOV and provided a more relevant calibration space. To fill the FOVs for the nonstandard cameras, a 12×12-in. dual plane calibration target was rotated 45°, aligning the target with the camera sensors (see Figure 8). Note that the views of the calibration target, shown in Figure 9, are rotated 90° relative to each other, whereas the standard stereo PIV targets are 180° relative to one another. DaVis uses the fiducial marks at the center of the target to determine the target orientation. The stereo calibrations were all $x^3y^3z^2$ order.

A calibration verification operation was performed using test images before the first stereo PIV run and later using actual PIV image data from a downstream axial location. The in-house routine Calverify procedure was performed on sample particle images to refine the light sheet alignment. Having continuous seed and no flare light in the images simplified the calibration verification process. The most recent version of Calverify enables the user to set the standard deviation value for removing outliers from the average vector maps; a standard deviation of 2 was used. Fifty images were used.

Both cross-stream PIV setups were used during the test, the nonstandard PIVxb setup only being acquired during measurements of external plug configurations.

The other factor making these measurements difficult was that the laser light impacting the plug is unavoidably being scattered back toward the cameras. This again reduces the regions where particles can be properly illuminated as the intersection of the plug and light sheet has a light intensity that saturates the cameras and particles cannot be imaged next to the plug. In fact, the scattering of the laser light from the particles usually illuminates the nozzle even when the light sheet is downstream of the nozzle hardware, producing a background image that can degrade the signal-to-noise ratio of the image in ring-like

patterns. LogLUT (logarithmic look-up table) scaling of the image intensity helps improve the dynamic range of the image, compressing the laser flare portion of the range and maximizing the region of the flow where measurement can be made.

For the traditional stereo PIV configuration, the data were processed using the in-house code PivBatch, using 64×64 pixel subregions on a 32×32 pixel grid for the first pass and then using six passes (simulated annealing) at 32×32 pixel resolution on a 16×16 grid, and two final passes using subregion distortion processing with 32×32 pixel subregions on a 16×16 pixel grid. Both symmetric phase-only filtering (SPOF) and LogLUT image intensity adjustments were used in the processing.

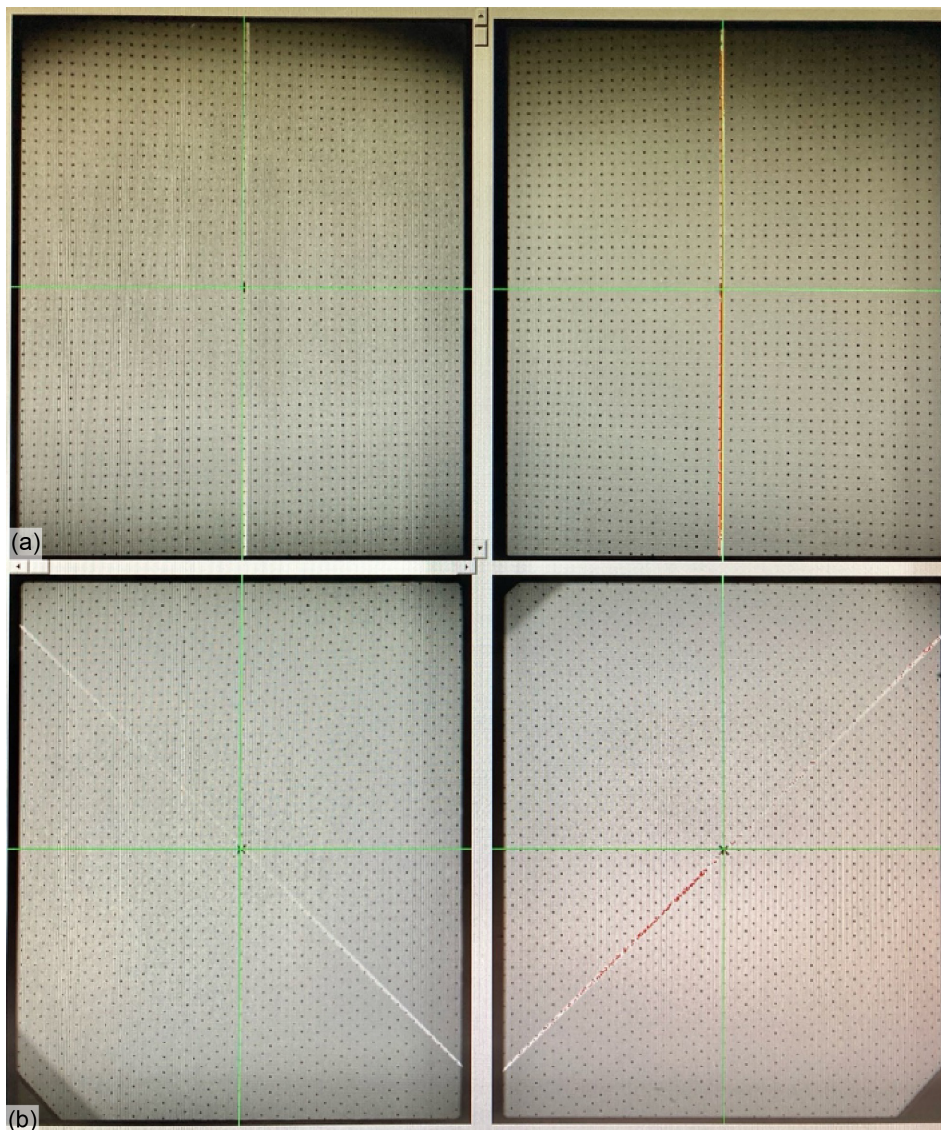


Figure 8.—Calibration target images. Red laser line is vertical in facility. (a) Traditional stereo PIV configuration (PIVxa). (b) Nonstandard stereo PIV configuration (PIVxb).

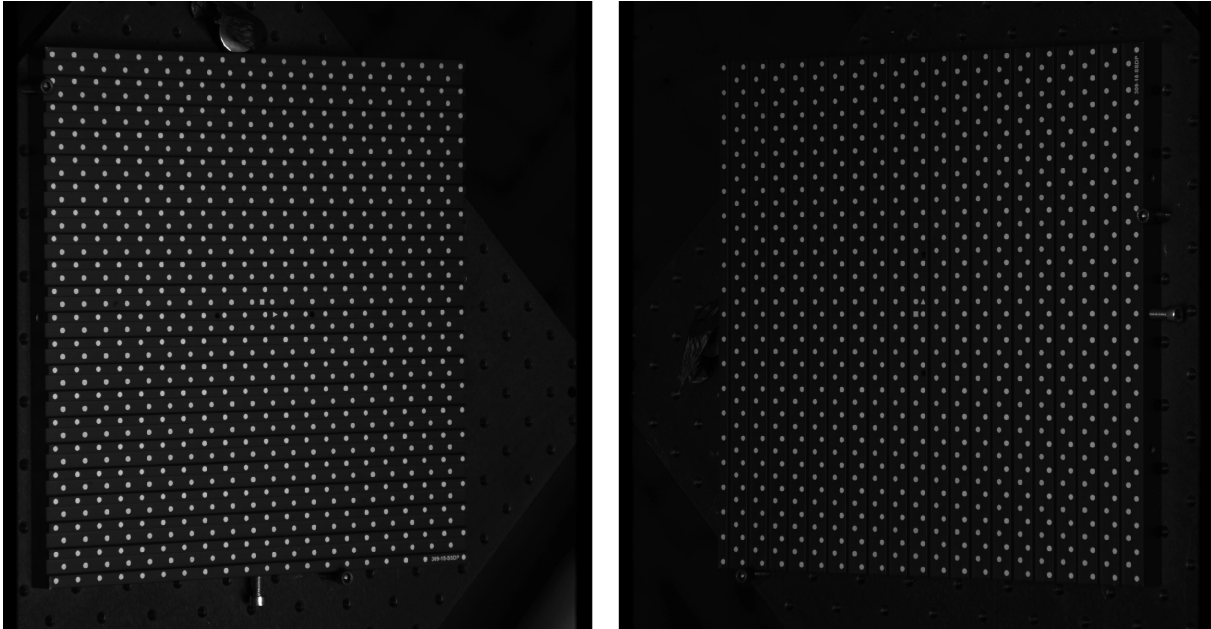


Figure 9.—Rotated calibration targets for PIVxb configuration.

The cross-stream PIV data were acquired at the axial stations shown in Table III and Figure 10. Acquisition of all measurement planes for a given flow condition constitutes a run and the rig was maintained on the setpoint for the duration of the run. For streamwise PIV, the run consists of seven acquisitions; for cross-stream PIV, a run consists of the five cross-stream axial locations. For both streamwise and cross-stream PIV configurations, 400 image pairs were acquired at every axial location. All locations in a run must be acquired while the rig is continuously running to avoid any matching issue between locations if the rig does not thermally grow exactly the same when heated and cooled.

When flow statistics were computed from the 400 independent samples at each spatial location, histograms of the velocity values were computed and velocities that lay outside the expected distribution as determined by Chauvenet's criterion were removed from the statistics. When presenting the results described later in this report, regions with more than 5 percent of their points being rejected have their values blanked, indicating unreliable data. These typically were caused by insufficient seed density in combination with lower light levels at the edges of the laser sheet.

In the datasets contained in this report, the data acquired using the traditional PIV setup (Figure 6) are denoted as PIVxa. Data acquired using the nonstandard PIV setup (Figure 7) are denoted as PIVxb. During analysis of the PIV data, discrepancies between the PIVxa and PIVxb measurements were noted. See the Results section for more details.

TABLE III.—PIV_x AXIAL STATIONS, RELATIVE TO NOZZLE EXIT

x , mm
10.2
25.4
102
254
508
1,016
1,905

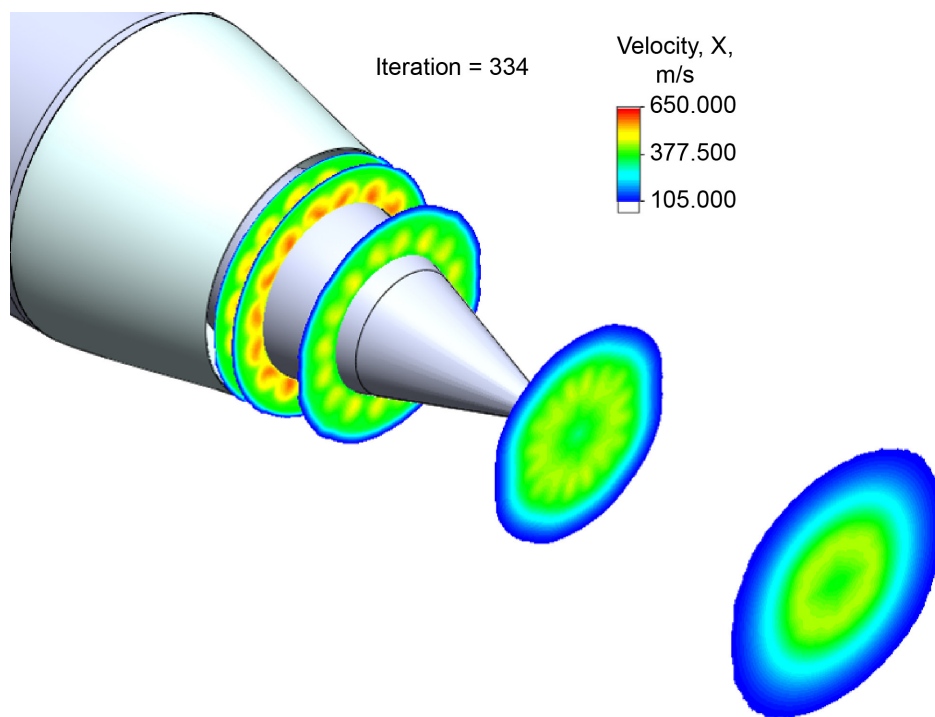


Figure 10.—Axial stations for PIV_x acquisitions as predicted by CFD.

Test Plan

Table IV contains the matrix of configurations and setpoints tested. As noted previously, not all flow conditions were run on all nozzle configurations. For instance, flow conditions with matched temperatures (setpoints 70, 71, 73, 75, and 4200) were not run on the lobed mixer with internal plug under the assumption that the result would be the same as the axisymmetric splitter. Setpoints 70 and 4200 were run on the lobed mixer with external plug; the lack of an internal wake validated the assumption that the lobed mixer made no difference. For variations in duct length (DS versus DL) and variations in plug length (p2069 versus p2079), only one dual-stream flow was measured.

TABLE IV.—PIV CONFIGURATIONS, MODEL CONFIGURATIONS, AND SETPOINTS ACQUIRED

	Configurations	Setpoints tested							
		1203	1200	3200	4200	70	71	73	75
PIVs	<i>Am0pInt</i>	1203	1200	3200	4200	70	71	73	75
	<i>Am5pInt</i>	1203	1200	3200	-----	---	---	---	---
	<i>DLM5p2069</i>	1203	1200	3200	4200	70	---	---	---
	<i>DSm5p2069</i>	1203	1200	-----	-----	---	---	---	---
	<i>DLM5p2079</i>	1203	1200	-----	-----	70	---	---	---
PIVxa	<i>Am0pInt</i>	-----	1200	-----	-----	---	---	---	---
	<i>Am5pInt</i>	-----	1200	-----	-----	---	---	---	---
	<i>DLM5p2069</i>	-----	1200	-----	-----	---	---	---	---
	<i>DSm5p2069</i>	-----	1200	-----	-----	---	---	---	---
PIVxb	<i>DLM5p2069</i>	-----	1200	-----	-----	---	---	---	---
	<i>DSm5p2069</i>	-----	1200	-----	-----	---	---	---	---

The majority of points were acquired only with streamwise PIV (PIVs). Cross-stream PIV (PIVxa and PIVxb) data were acquired only on four of the configurations, and only with the dual-stream setpoint 1200. Cross-stream measurements on the long plug were not acquired as the focus of these measurements was on the mixing internal to the nozzle.

Results

Data analysis is ongoing at the time of this report, but a basic quality control pass has been made on the data.

Streamwise PIV (PIVs)

Figure 11 to Figure 31 provide a visual catalog of streamwise statistics acquired and included in the data files of the appendixes. For each configuration and flow condition, two-component statistics are available in the streamwise PIV. Quantities given are

$$\text{Mean axial velocity:} \quad U(x, y) = \frac{1}{N} \sum_i^N u_i(x, y)$$

$$\text{Mean vertical velocity:} \quad V(x, y) = \frac{1}{N} \sum_i^N v_i(x, y)$$

$$\text{Autocovariance of axial velocity:} \quad u'u'(x, y) = \frac{1}{N-1} \sum_i^N (u_i - U)^2$$

$$\text{Autocovariance of vertical velocity:} \quad v'v'(x, y) = \frac{1}{N-1} \sum_i^N (v_i - V)^2$$

$$\text{Covariance of axial and vertical velocity:} \quad u'v'(x, y) = \frac{1}{N-1} \sum_i^N (u_i - U)(v_i - V)$$

$$\text{Quality:} \quad N(x, y)/400$$

where i denotes an instantaneous velocity measurement at a point (x, y) , and N is the number of samples that passed Chauvenet's criterion for judging outlying points out of the 400 acquired at each location. Although this formally requires assuming that the samples have a normal distribution, in practice, outliers

are found in regions where there is too little seed or interfering background illumination. Application of Chauvenet's criterion is an unbiased way to identify these regions by ignoring regions where the quality metric is low. For instance, in the plots included in this report, regions with quality less than 0.95 are blanked.

There are several processing artifacts observable in the data of which a user should be aware. The merged vector maps from the 2x2 camera configuration sometimes exhibited low data quality in the overlapped region. Several factors contribute to this: low seeding concentration in the ambient regions of the flow (on outer regions of the FOV), lack of illumination by the laser light sheet in the corners of the camera images (especially on the lower edge where the light fan is narrowest), and sticking electromechanical shutters on the cameras. Each camera is equipped with an electromechanical shutter to reduce the amount of ambient light recorded by the cameras. When a shutter sticks or closes too slowly, the particle image suffers from a poor signal-to-noise ratio. This malfunction is quite evident as bands of anomalies axially spaced 150 mm (the distance between cameras) or 300 mm (the distance between acquisitions) apart. These low signal-to-noise regions were usually constrained to the top and bottom areas of the FOVs, and mostly affected the 2nd-order statistics, even when the quality metric itself was only slightly affected. User beware.

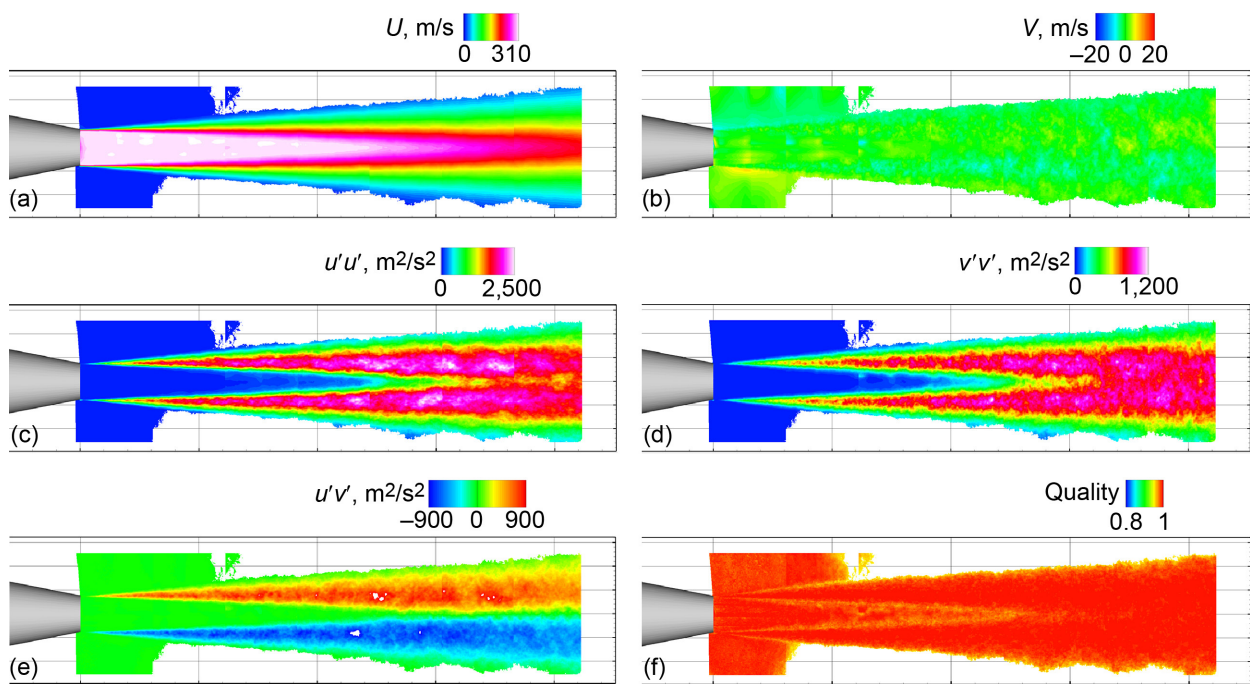


Figure 11.—Streamwise turbulent velocity statistics for *Am0plnt*, setpoint 0070. (a) U , m/s. (b) V , m/s. (c) $u'u'$, m^2/s^2 . (d) $v'v'$, m^2/s^2 . (e) $u'v'$, m^2/s^2 . (f) Quality.

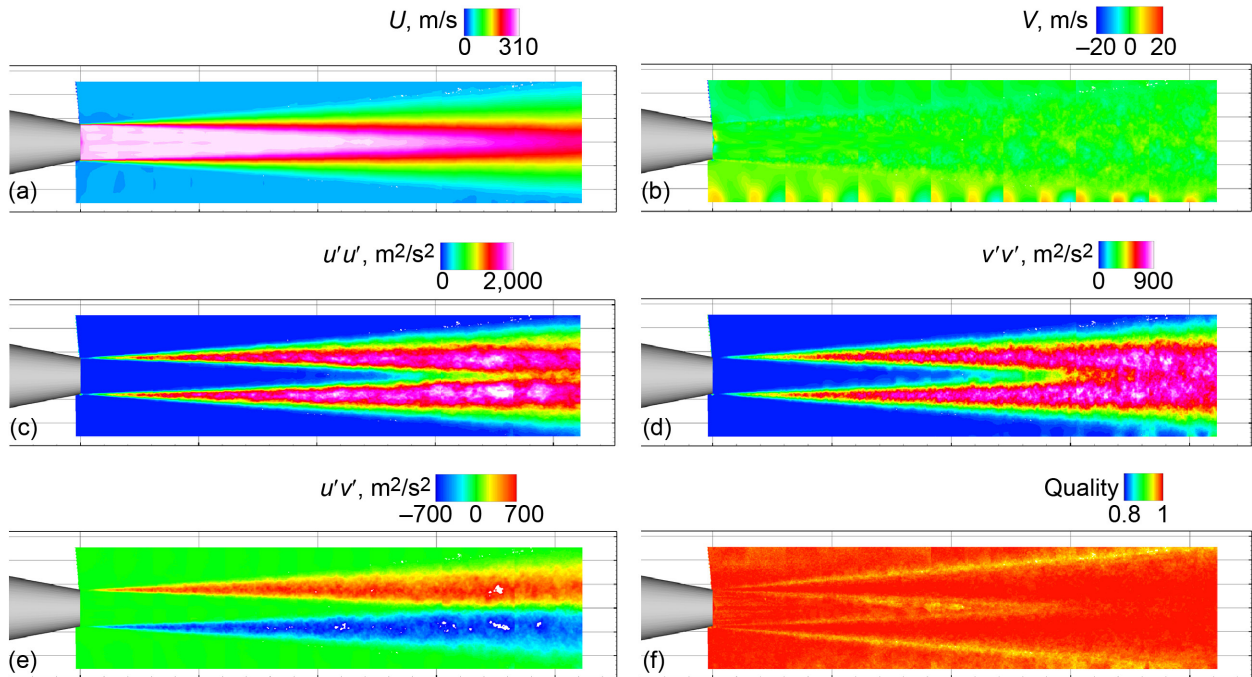


Figure 12.—Streamwise turbulent velocity statistics for *Am0plnt*, setpoint 0071. (a) U , m/s. (b) V , m/s. (c) $u'u'$, m^2/s^2 . (d) $v'v'$, m^2/s^2 . (e) $u'v'$, m^2/s^2 . (f) Quality.

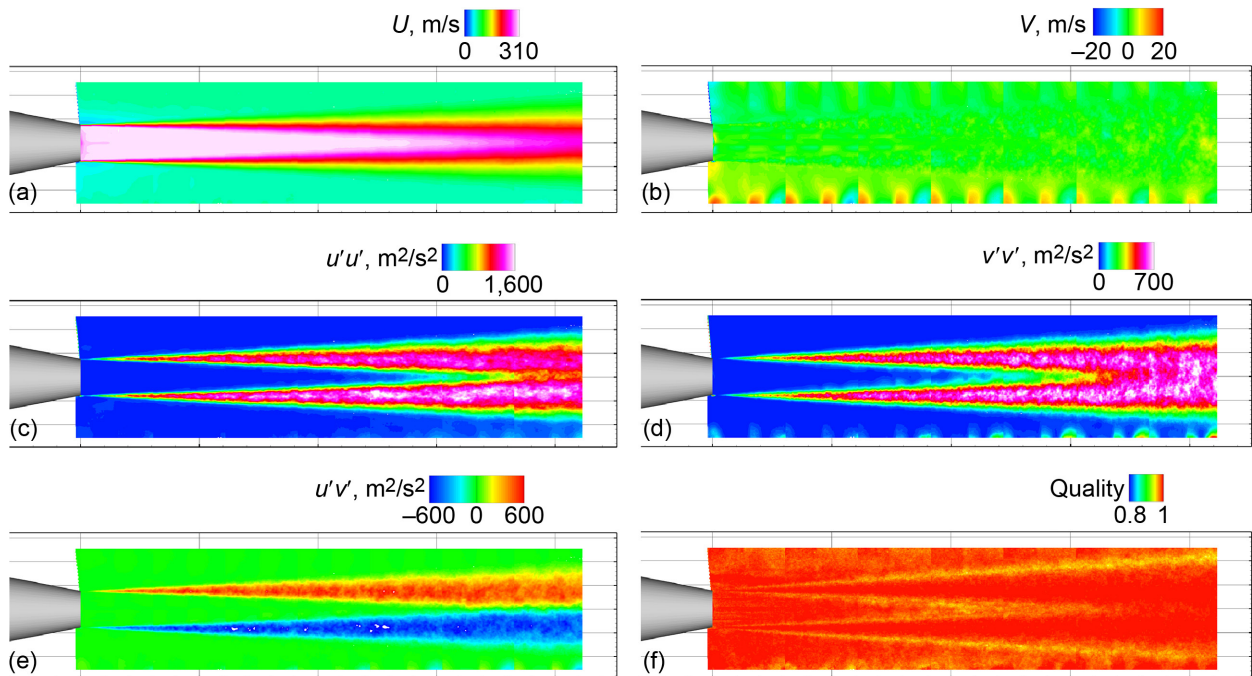


Figure 13.—Streamwise turbulent velocity statistics for *Am0plnt*, setpoint 0073. (a) U , m/s. (b) V , m/s. (c) $u'u'$, m^2/s^2 . (d) $v'v'$, m^2/s^2 . (e) $u'v'$, m^2/s^2 . (f) Quality.

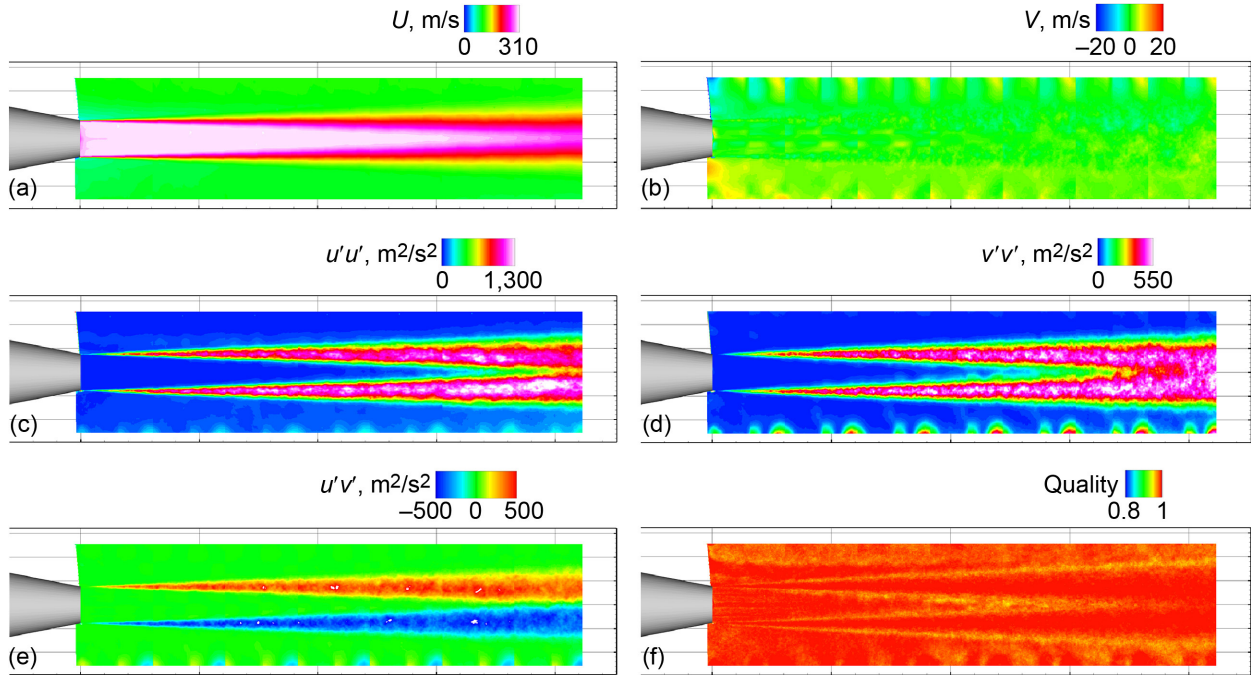


Figure 14.—Streamwise turbulent velocity statistics for *Am0plnt*, setpoint 0075. (a) U , m/s. (b) V , m/s. (c) $u'u'$, m^2/s^2 . (d) $v'v'$, m^2/s^2 . (e) $u'v'$, m^2/s^2 . (f) Quality.

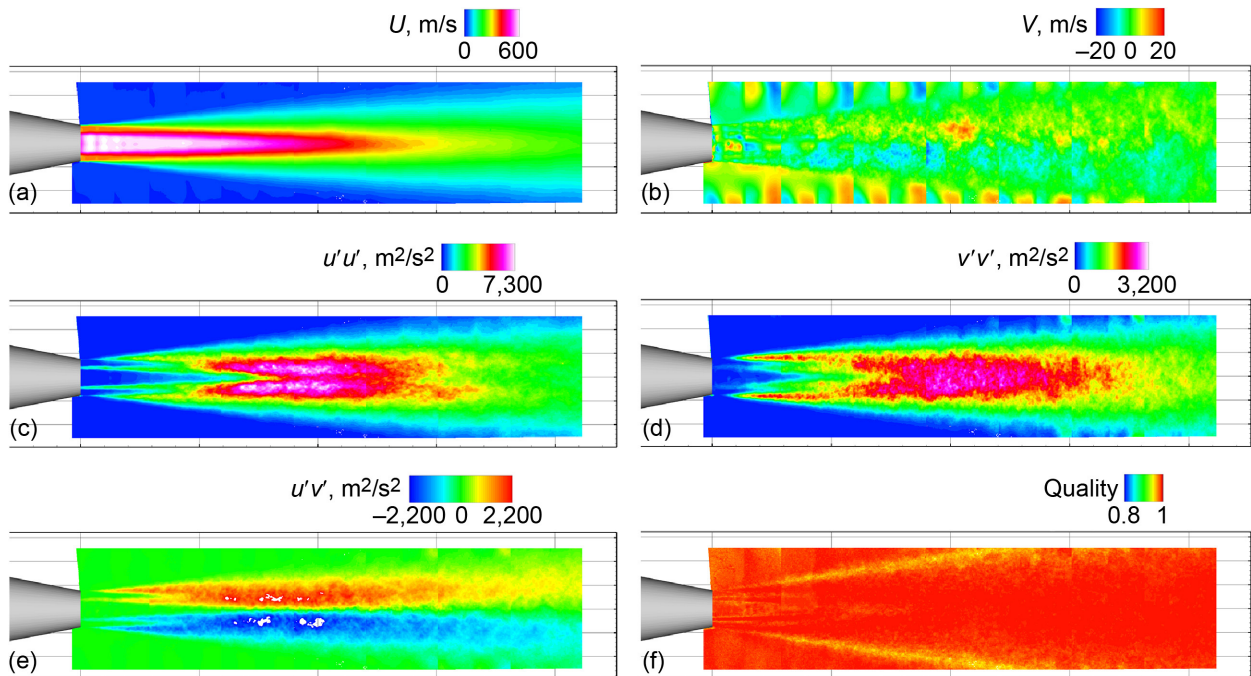


Figure 15.—Streamwise turbulent velocity statistics for *Am0plnt*, setpoint 1200. (a) U , m/s. (b) V , m/s. (c) $u'u'$, m^2/s^2 . (d) $v'v'$, m^2/s^2 . (e) $u'v'$, m^2/s^2 . (f) Quality.

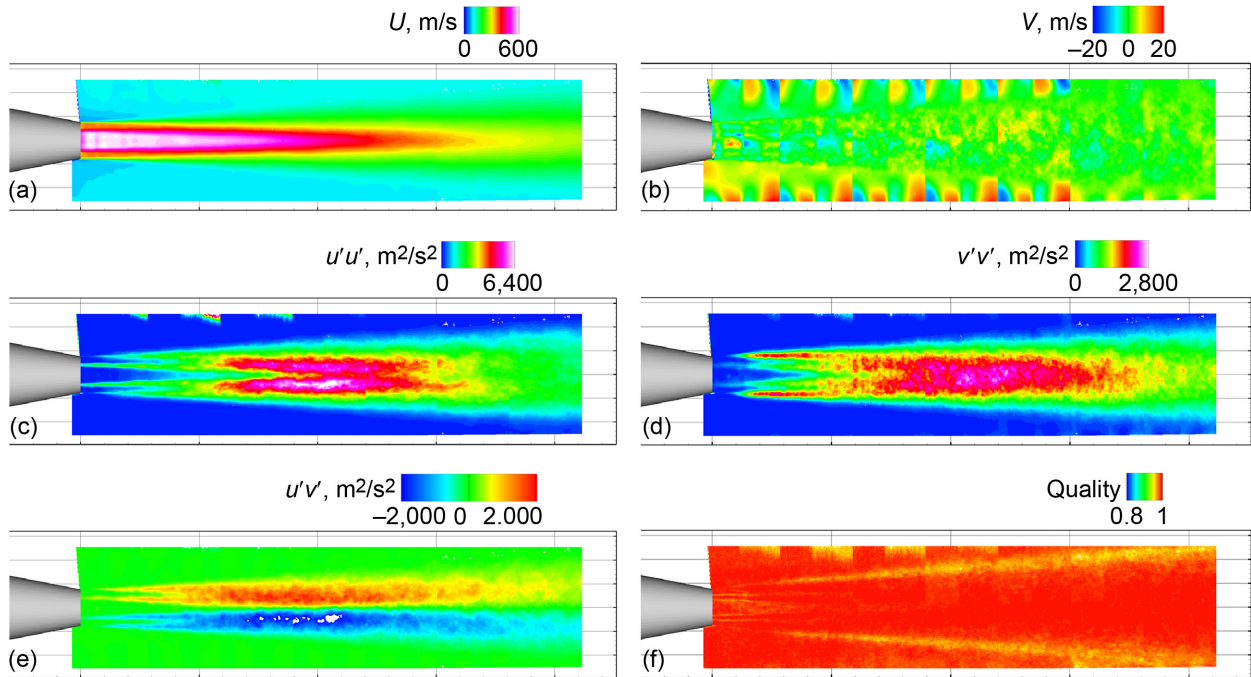


Figure 16.—Streamwise turbulent velocity statistics for *Am0plnt*, setpoint 1203. (a) U , m/s. (b) V , m/s. (c) $u'u'$, m^2/s^2 . (d) $v'v'$, m^2/s^2 . (e) $u'v'$, m^2/s^2 . (f) Quality.

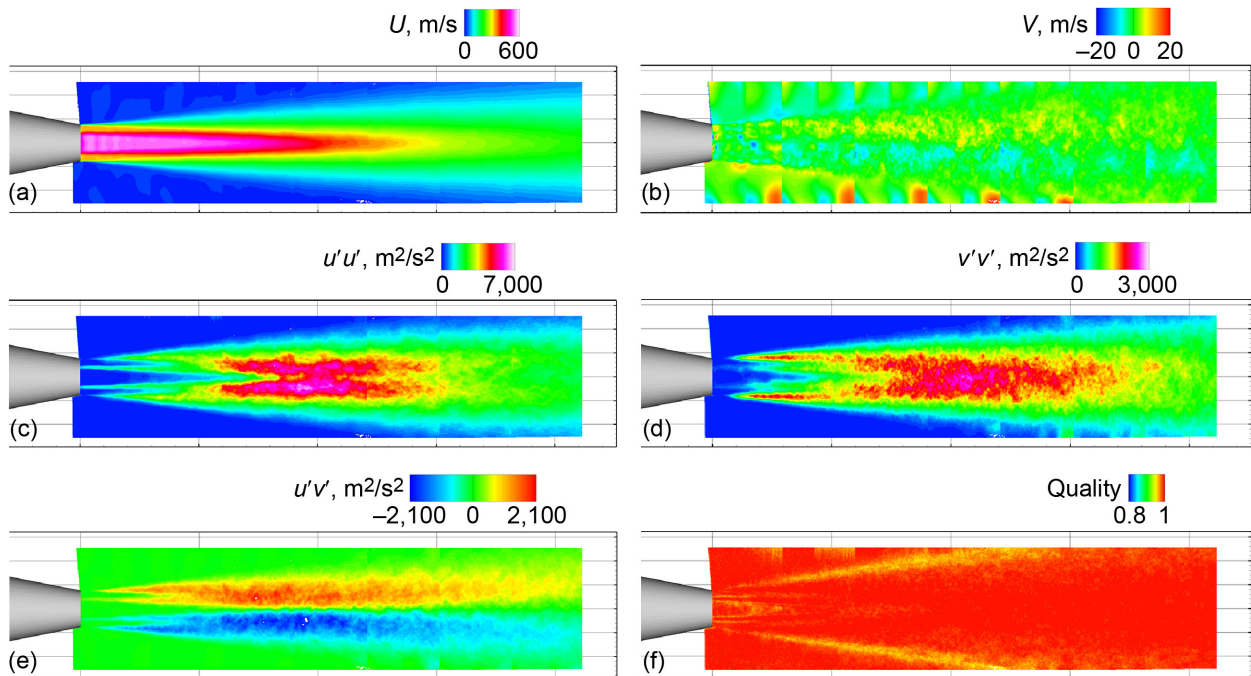


Figure 17.—Streamwise turbulent velocity statistics for *Am0plnt*, setpoint 3200. (a) U , m/s. (b) V , m/s. (c) $u'u'$, m^2/s^2 . (d) $v'v'$, m^2/s^2 . (e) $u'v'$, m^2/s^2 . (f) Quality.

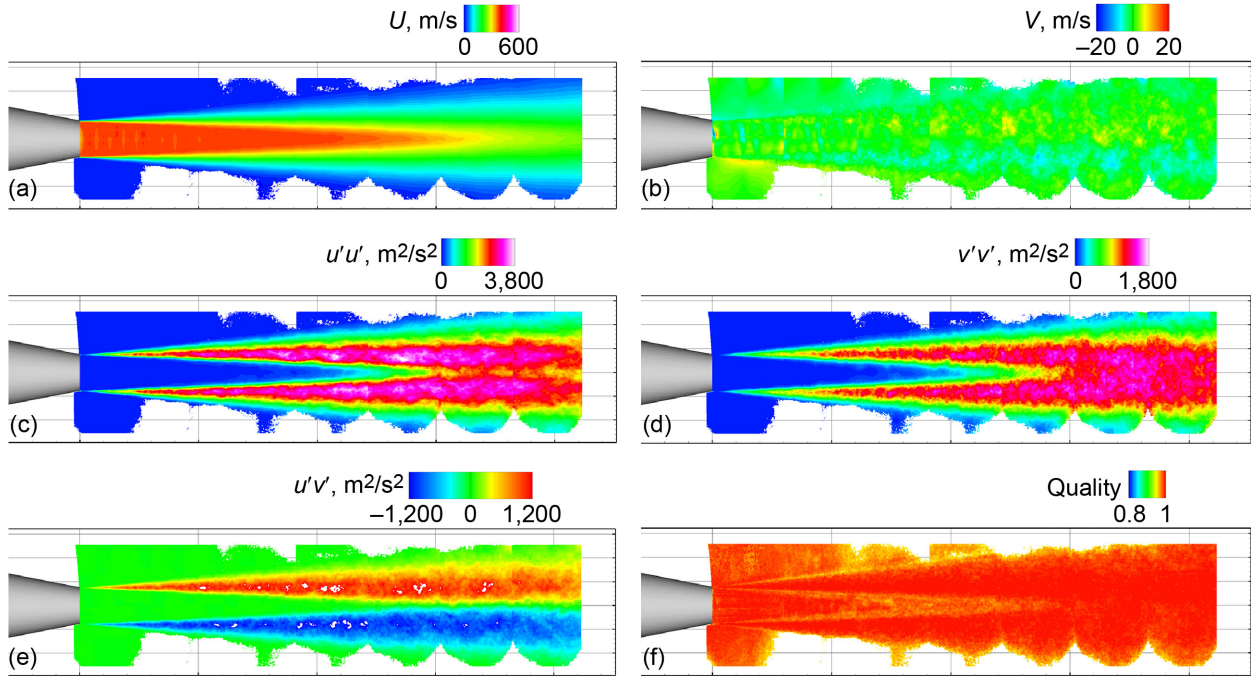


Figure 18.—Streamwise turbulent velocity statistics for *Am0plnt*, setpoint 4200. (a) U , m/s. (b) V , m/s. (c) $u'u'$, m^2/s^2 . (d) $v'v'$, m^2/s^2 . (e) $u'v'$, m^2/s^2 . (f) Quality.

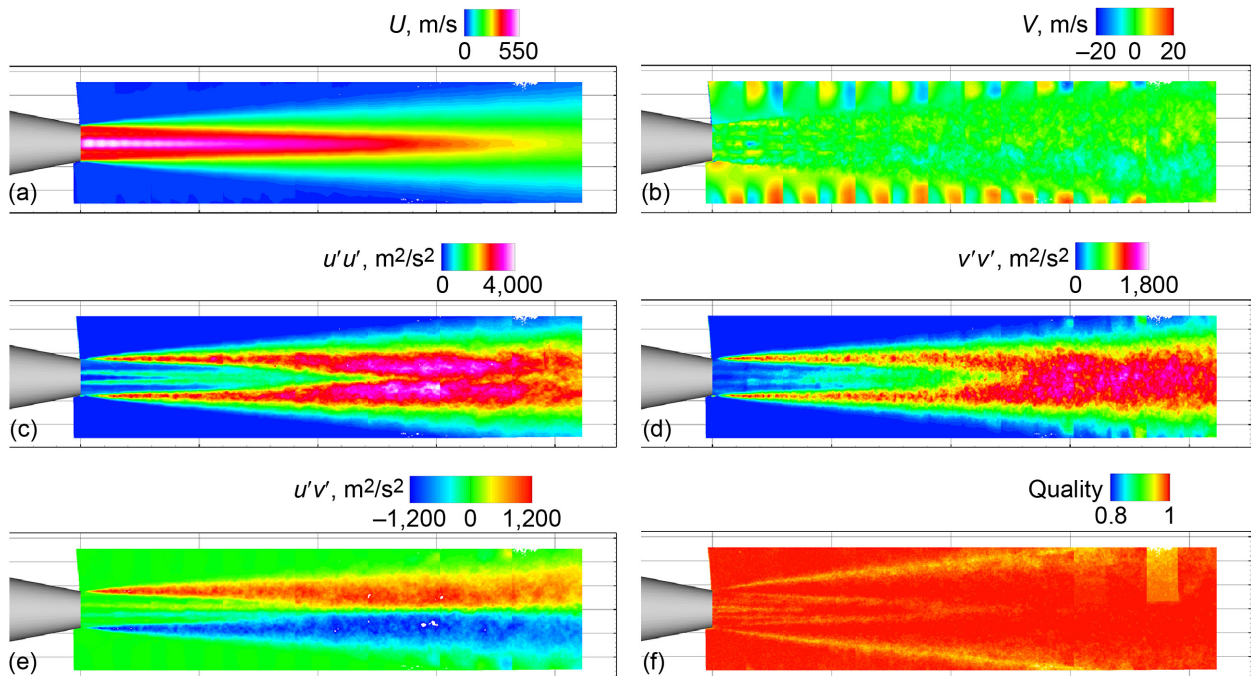


Figure 19.— Streamwise turbulent velocity statistics for *Am5plnt*, setpoint 3200. (a) U , m/s. (b) V , m/s. (c) $u'u'$, m^2/s^2 . (d) $v'v'$, m^2/s^2 . (e) $u'v'$, m^2/s^2 . (f) Quality.

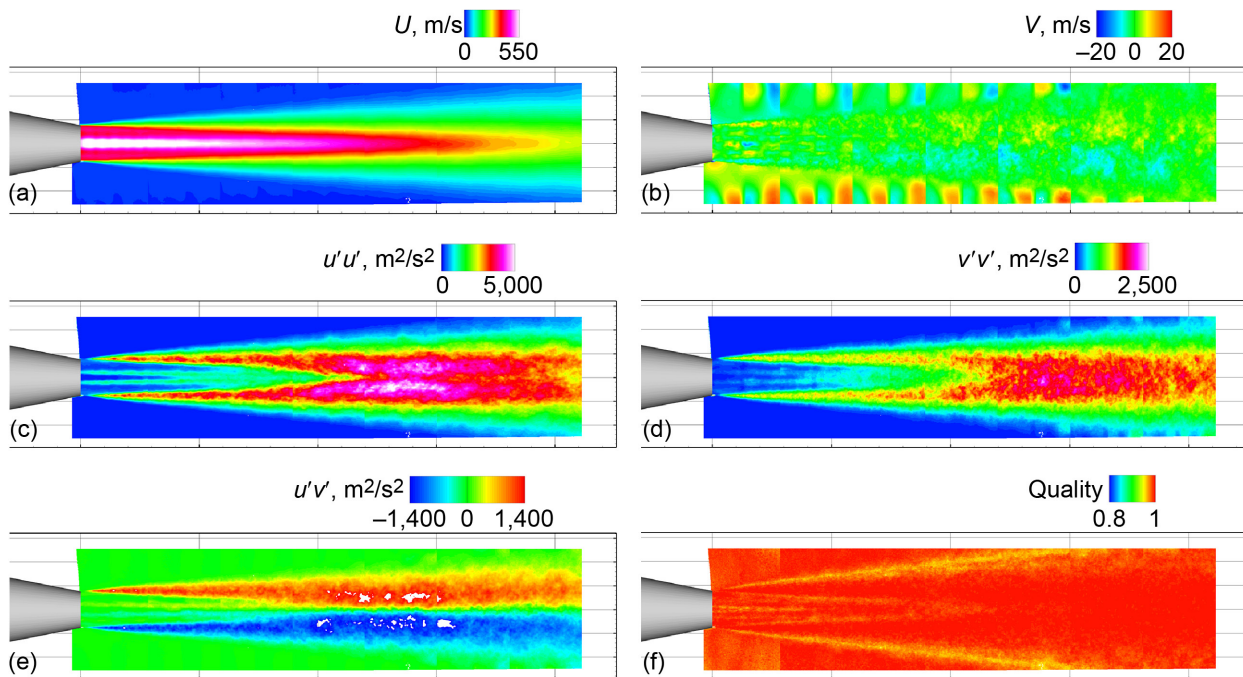


Figure 20.—Streamwise turbulent velocity statistics for *Am5plnt*, setpoint 1200. (a) U , m/s. (b) V , m/s. (c) $u'u'$, m^2/s^2 . (d) $v'v'$, m^2/s^2 . (e) $u'v'$, m^2/s^2 . (f) Quality.

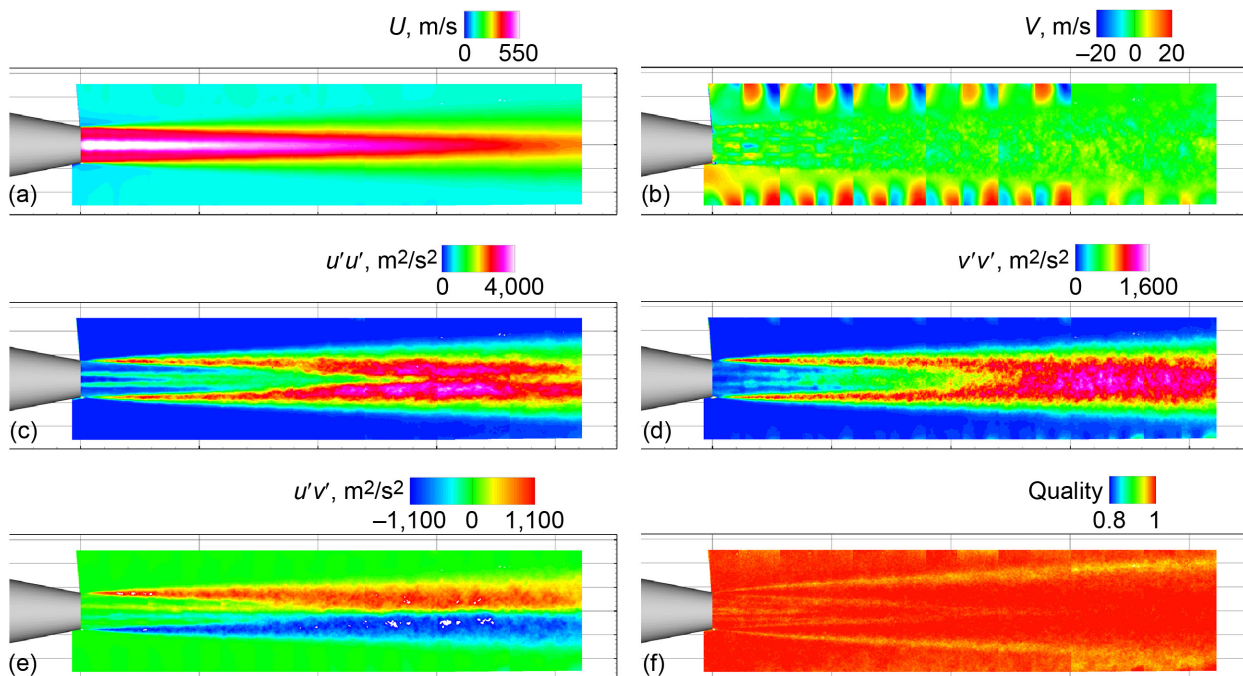


Figure 21.—Streamwise turbulent velocity statistics for *Am5plnt*, setpoint 1203. (a) U , m/s. (b) V , m/s. (c) $u'u'$, m^2/s^2 . (d) $v'v'$, m^2/s^2 . (e) $u'v'$, m^2/s^2 . (f) Quality.

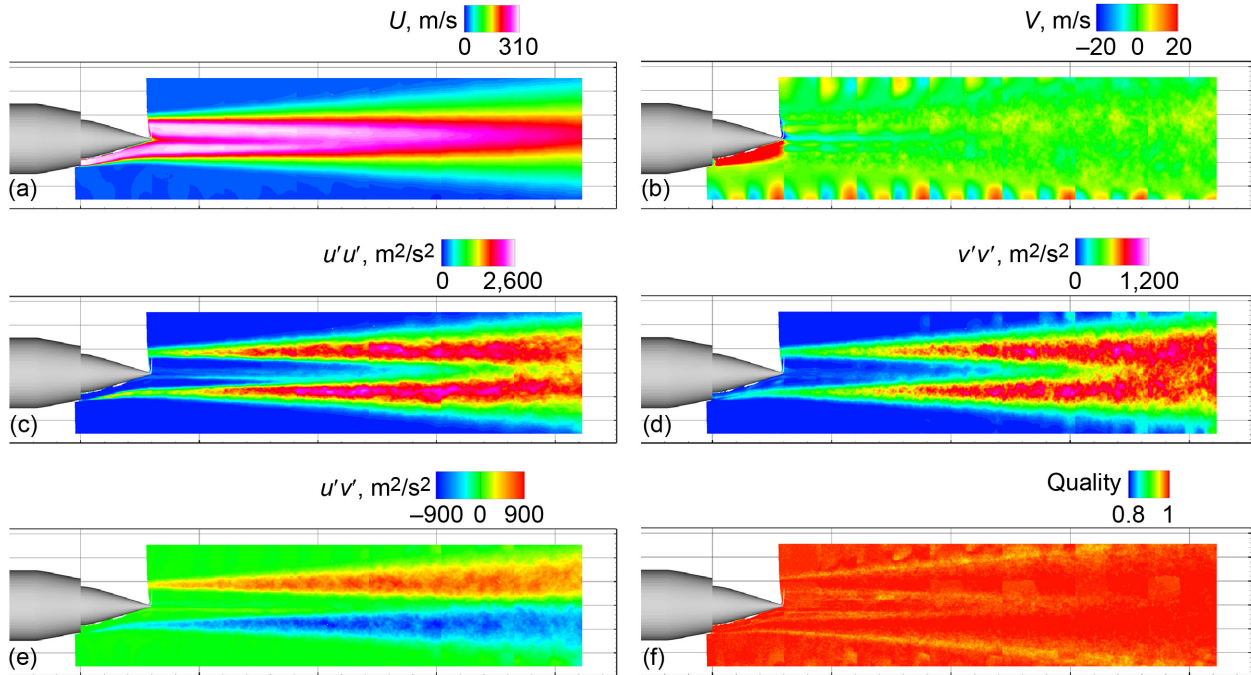


Figure 22.—Streamwise turbulent velocity statistics for *DLM5p2069*, setpoint 0070. (a) U , m/s. (b) V , m/s. (c) $u'u'$, m^2/s^2 . (d) $v'v'$, m^2/s^2 . (e) $u'v'$, m^2/s^2 . (f) Quality.

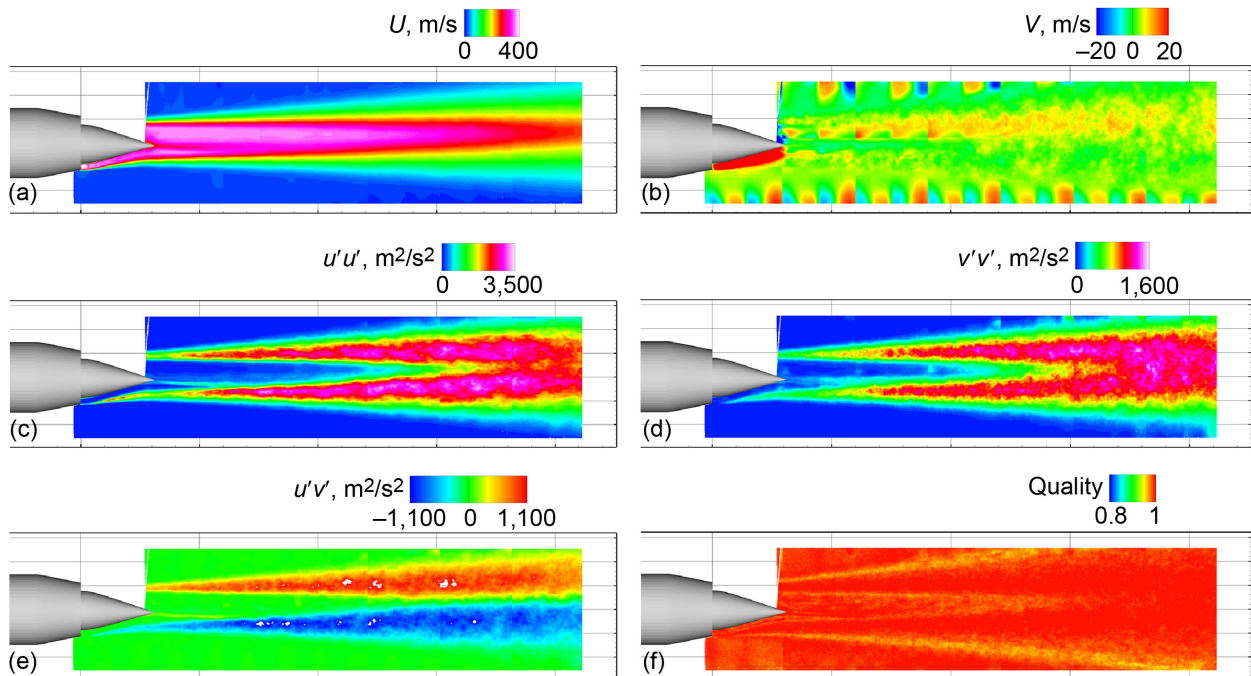


Figure 23.—Streamwise turbulent velocity statistics for *DLM5p2069*, setpoint 4200. (a) U , m/s. (b) V , m/s. (c) $u'u'$, m^2/s^2 . (d) $v'v'$, m^2/s^2 . (e) $u'v'$, m^2/s^2 . (f) Quality.

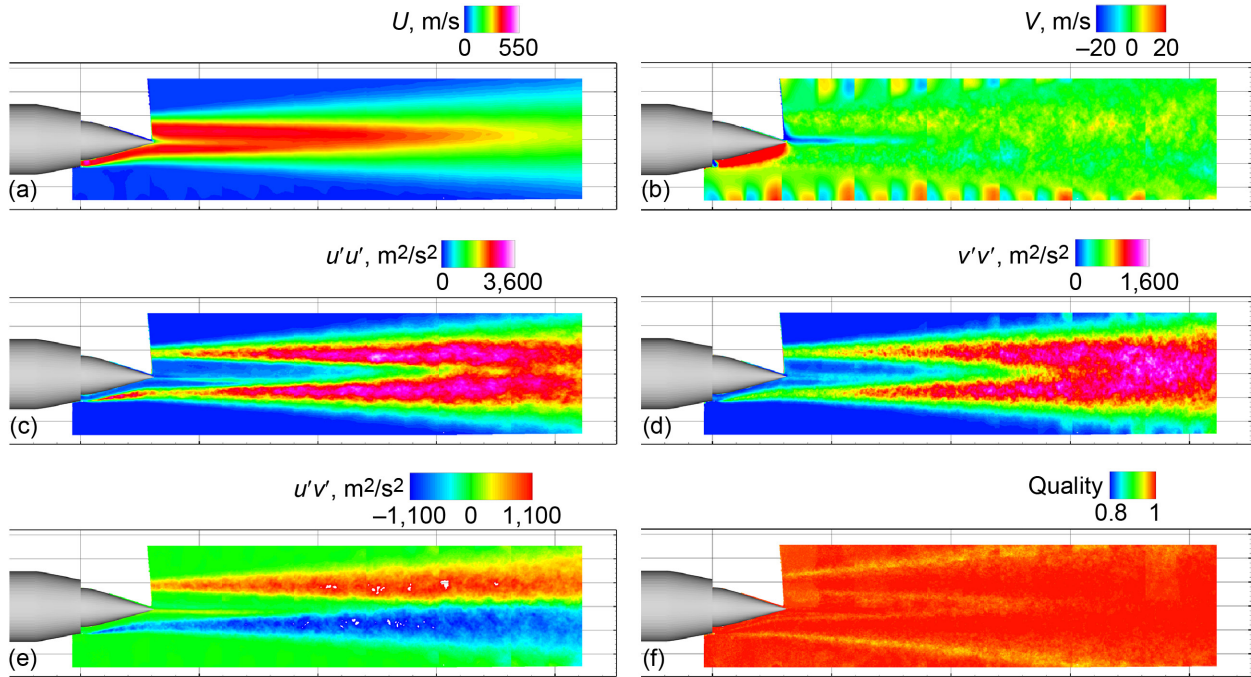


Figure 24.—Streamwise turbulent velocity statistics for *DLM5p2069*, setpoint 3200. (a) U , m/s. (b) V , m/s. (c) $u'u'$, m^2/s^2 . (d) $v'v'$, m^2/s^2 . (e) $u'v'$, m^2/s^2 . (f) Quality.

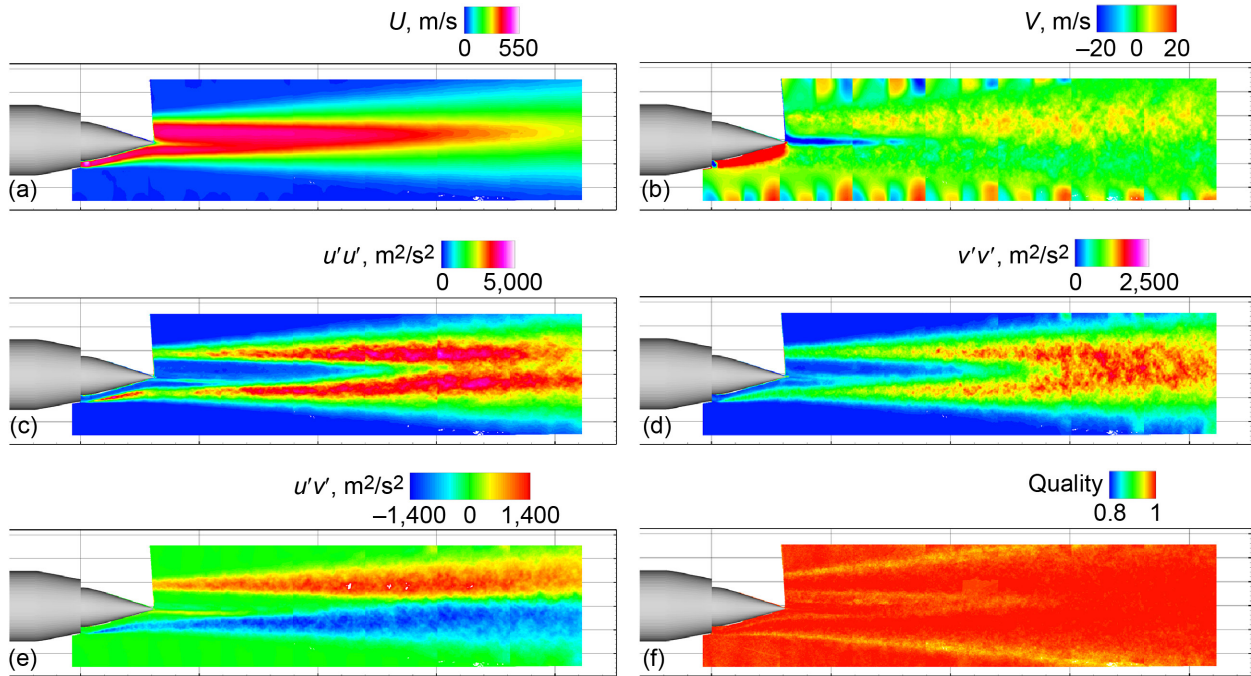


Figure 25.—Streamwise turbulent velocity statistics for *DLM5p2069*, setpoint 1200. (a) U , m/s. (b) V , m/s. (c) $u'u'$, m^2/s^2 . (d) $v'v'$, m^2/s^2 . (e) $u'v'$, m^2/s^2 . (f) Quality.

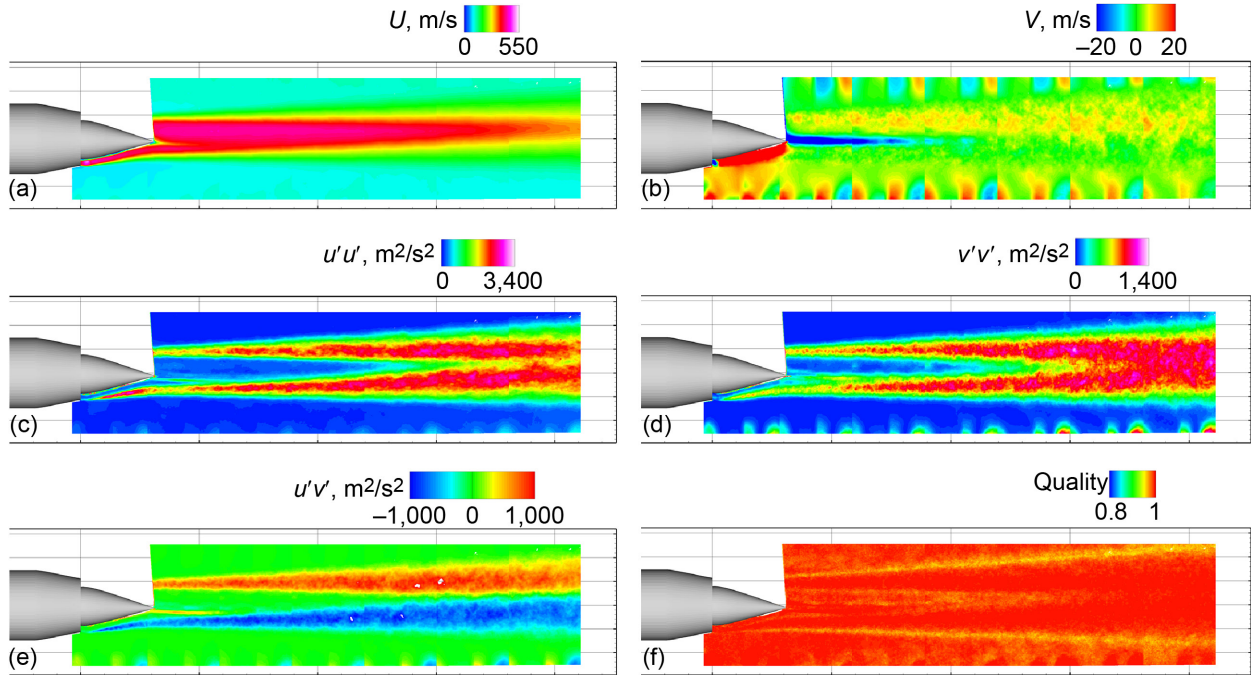


Figure 26.—Streamwise turbulent velocity statistics for *DLM5p2069*, setpoint 1203. (a) U , m/s. (b) V , m/s. (c) $u'u'$, m^2/s^2 . (d) $v'v'$, m^2/s^2 . (e) $u'v'$, m^2/s^2 . (f) Quality.

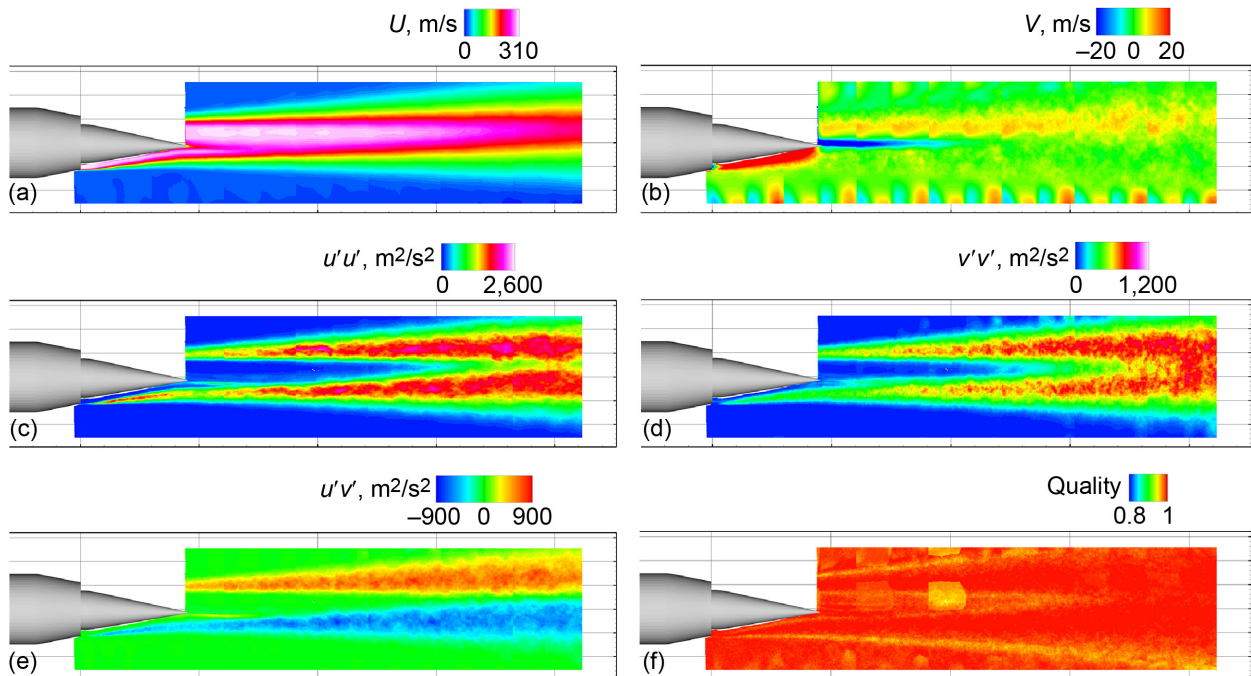


Figure 27.—Streamwise turbulent velocity statistics for *DLM5p2079*, setpoint 0070. (a) U , m/s. (b) V , m/s. (c) $u'u'$, m^2/s^2 . (d) $v'v'$, m^2/s^2 . (e) $u'v'$, m^2/s^2 . (f) Quality.

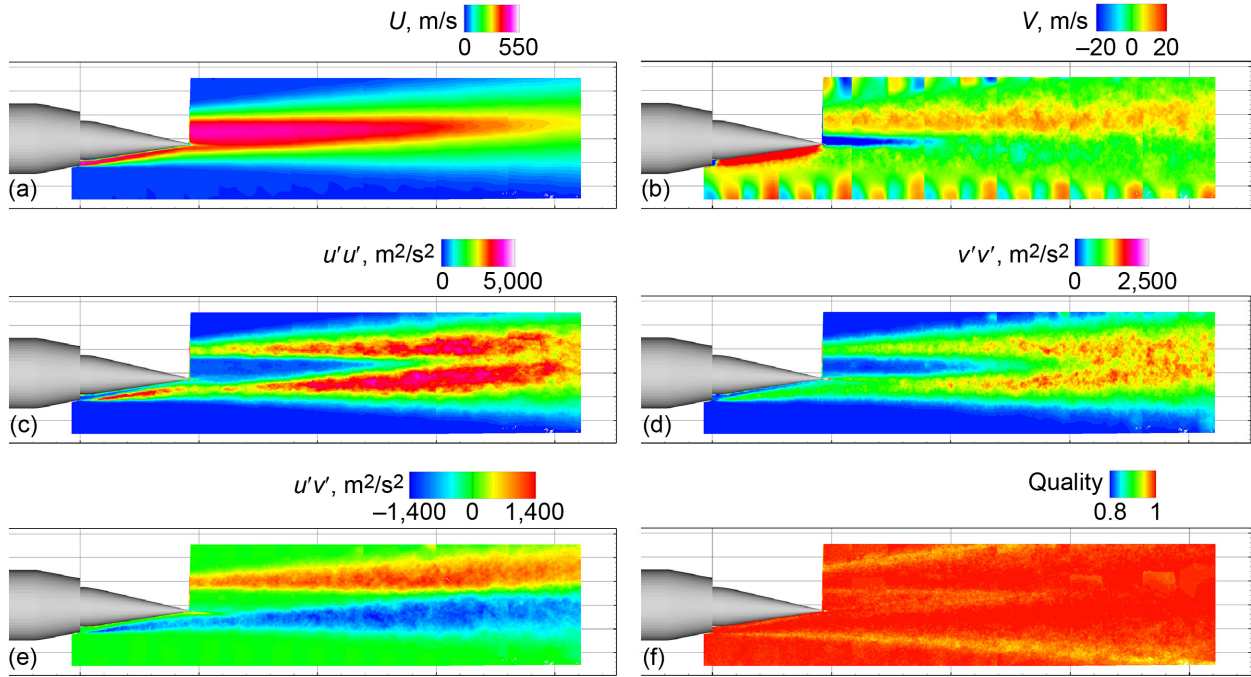


Figure 28.—Streamwise turbulent velocity statistics for *DLM5p2079*, setpoint 1200. (a) U , m/s. (b) V , m/s. (c) $u'u'$, m^2/s^2 . (d) $v'v'$, m^2/s^2 . (e) $u'v'$, m^2/s^2 . (f) Quality.

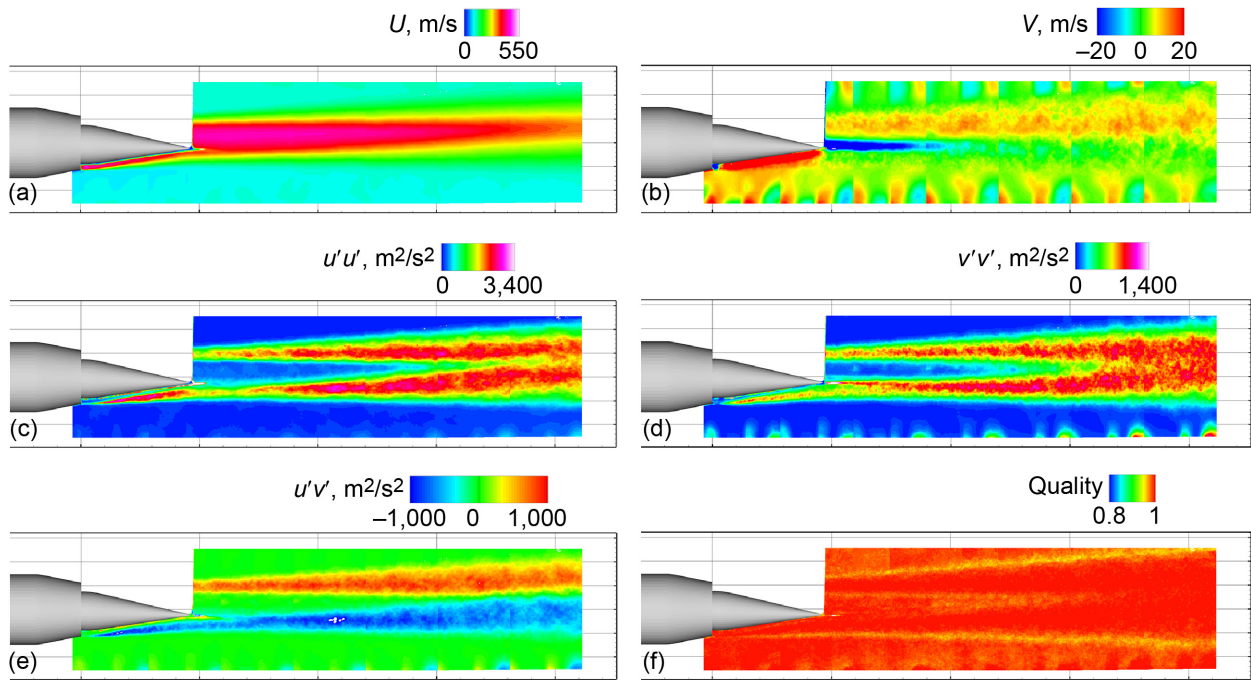


Figure 29.—Streamwise turbulent velocity statistics for *DLM5p2079*, setpoint 1203. (a) U , m/s. (b) V , m/s. (c) $u'u'$, m^2/s^2 . (d) $v'v'$, m^2/s^2 . (e) $u'v'$, m^2/s^2 . (f) Quality.

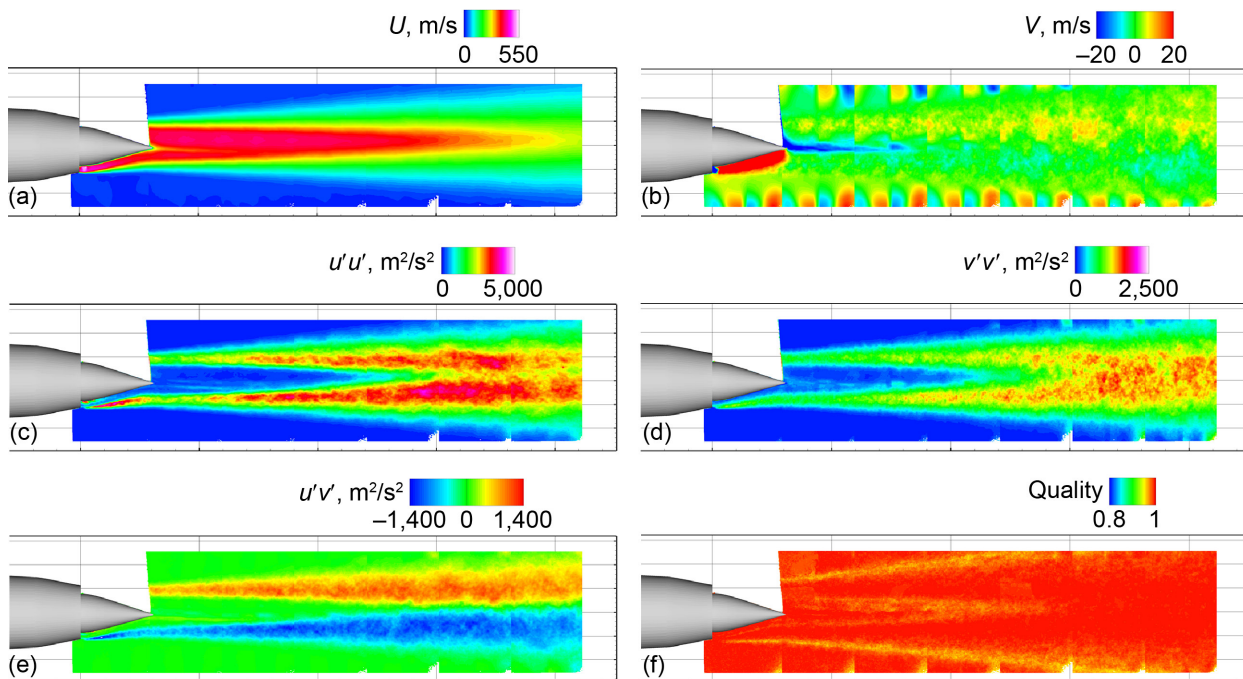


Figure 30.—Streamwise turbulent velocity statistics for *DSM5p2069*, setpoint 1200. (a) U , m/s. (b) V , m/s. (c) $u'u'$, m^2/s^2 . (d) $v'v'$, m^2/s^2 . (e) $u'v'$, m^2/s^2 . (f) Quality.

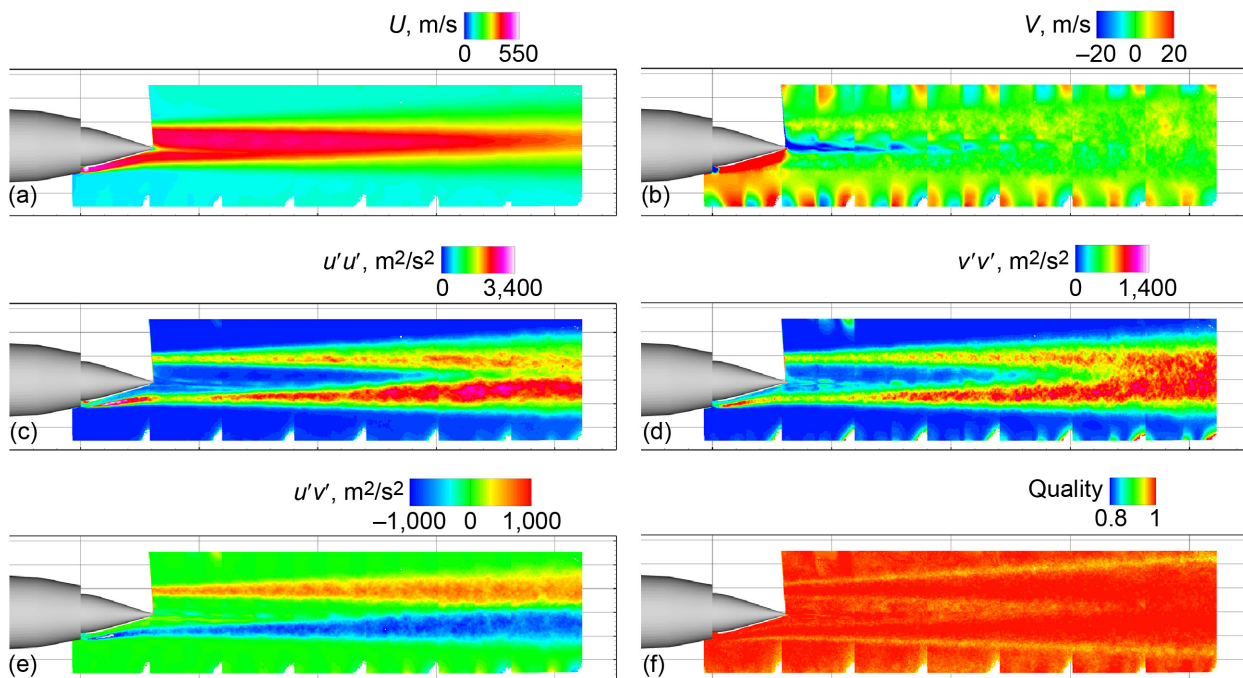


Figure 31.—Streamwise turbulent velocity statistics for *DSM5p2069*, setpoint 1203. (a) U , m/s. (b) V , m/s. (c) $u'u'$, m^2/s^2 . (d) $v'v'$, m^2/s^2 . (e) $u'v'$, m^2/s^2 . (f) Quality.

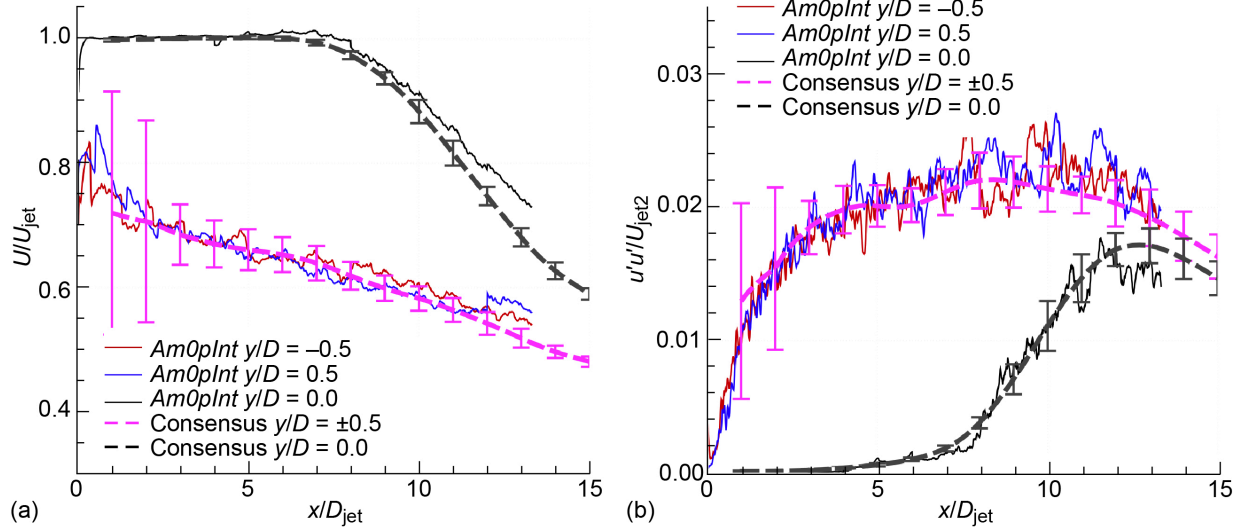


Figure 32.—Comparison of centerline and lipline statistics for unheated $Ma=0.9$, current test versus established database. (a) Mean axial velocity. (b) Autocovariance of axial velocity.

As a simple check against established data, Figure 32 shows the current measurement of an unheated $Ma = 0.9$ jet ($Am0pInt$, setpoint 0070) plotted against previously documented datasets from a similar, but much smaller jet (SMC000, setpoint 7). First, the internal plug configuration did not have significant asymmetry of the nozzle geometry as verified by comparing the mean and autocovariance of the axial velocity on the liplines. Second, the independence of these results on scale and rig can be checked by how well the previous results overlay the current data. Note that to obtain data on the lipline the current dataset has been interpolated onto lines of constant radius. Not only is the current plume very symmetric across the jet, but it also agrees with the Consensus dataset [9] to within the uncertainty bar established in the Consensus data for repeatability of PIV over five previous tests.

Cross-Stream PIV (PIV_x)

Cross-stream PIV was acquired using stereographic camera setups, allowing measurement of all three components of velocity. Thus, the turbulent statistics computed in the streamwise PIV is supplemented by these four statistics:

$$\text{Mean horizontal velocity: } W(x, y) = \frac{1}{N} \sum_i^N w_i(x, y)$$

$$\text{Autocovariance of horizontal velocity: } ww(x, y) = \frac{1}{N-1} \sum_i^N (w_i - W)^2$$

$$\text{Covariance of axial and horizontal velocity: } uw(x, y) = \frac{1}{N-1} \sum_i^N (u_i - U)(w_i - W)$$

$$\text{Covariance of vertical and horizontal velocity: } vw(x, y) = \frac{1}{N-1} \sum_i^N (v_i - V)(w_i - W)$$

Cross-stream PIV measurements were only made on one flow (setpoint 1200). Traditional cross-stream (PIV_{xa}) measurements were acquired on configurations $Am0pInt$, $Am5pInt$, $DLM5p2069$, and $DSm5p2069$. Nonstandard PIV_{xb} measurements were only acquired for the two external plug configurations, $DLM5p2069$ and $DSm5p2069$, where the nonstandard stereo PIV setup offered an increased FOV near the nozzle.

The results for the traditional stereo cross-stream PIV_{xa} measurements are catalogued in Figure 33 to Figure 36. In the figures, blanking has been applied when U (average axial velocity) is less than 20 m/s

and when the quality metric is less 0.95. Also, note that the PIVxa FOV truncates the datasets on the y - and z -borders in the downstream axial locations.

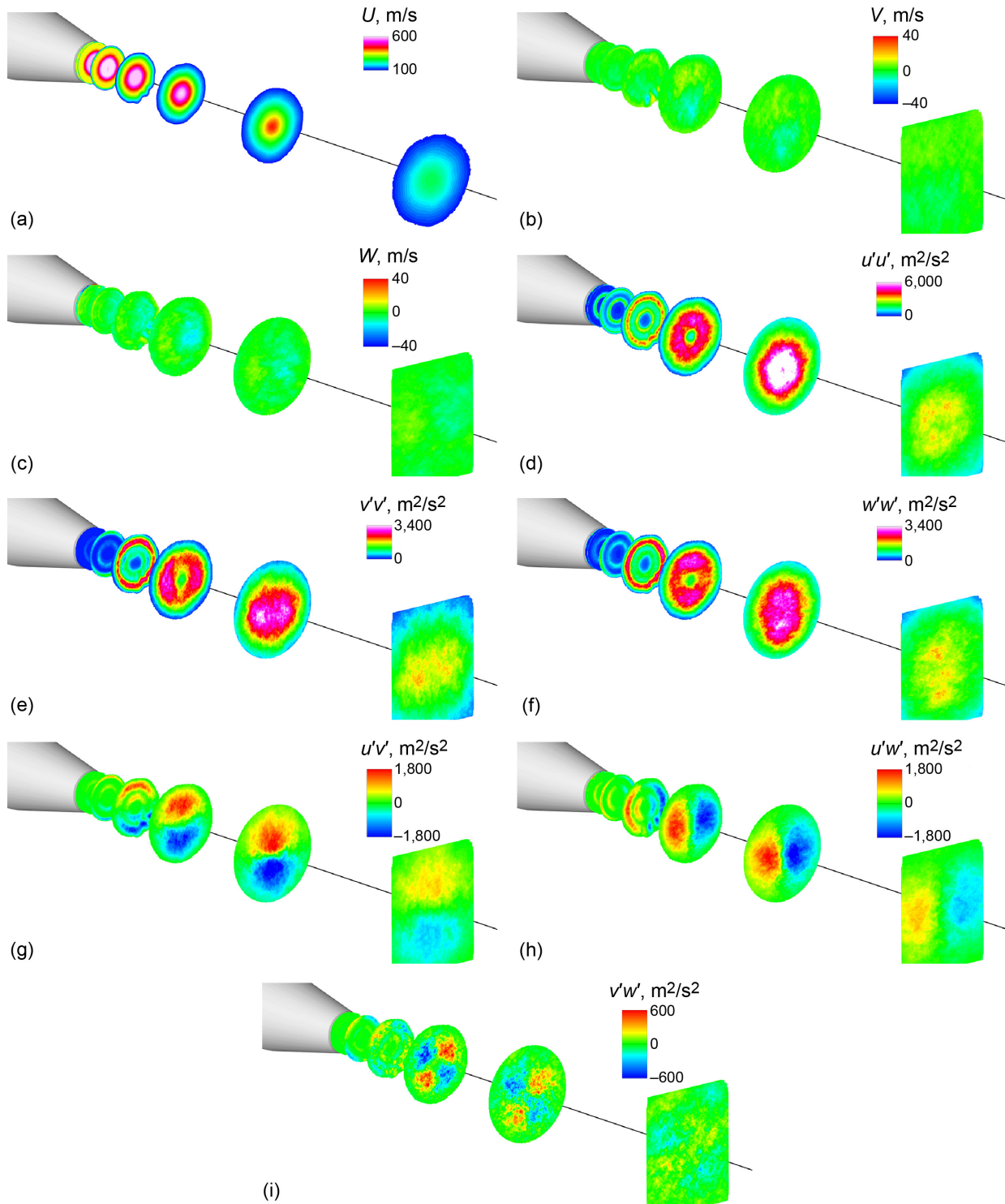


Figure 33.—Turbulent velocity statistics for *Am0plnt*, setpoint 1200, using PIVxa optics. (a) U , m/s. (b) V , m/s. (c) W , m/s. (d) $u'u'$, m^2/s^2 . (e) $v'v'$, m^2/s^2 . (f) $w'w'$, m^2/s^2 . (g) $u'v'$, m^2/s^2 . (h) $u'w'$, m^2/s^2 . (i) $v'w'$, m^2/s^2 .

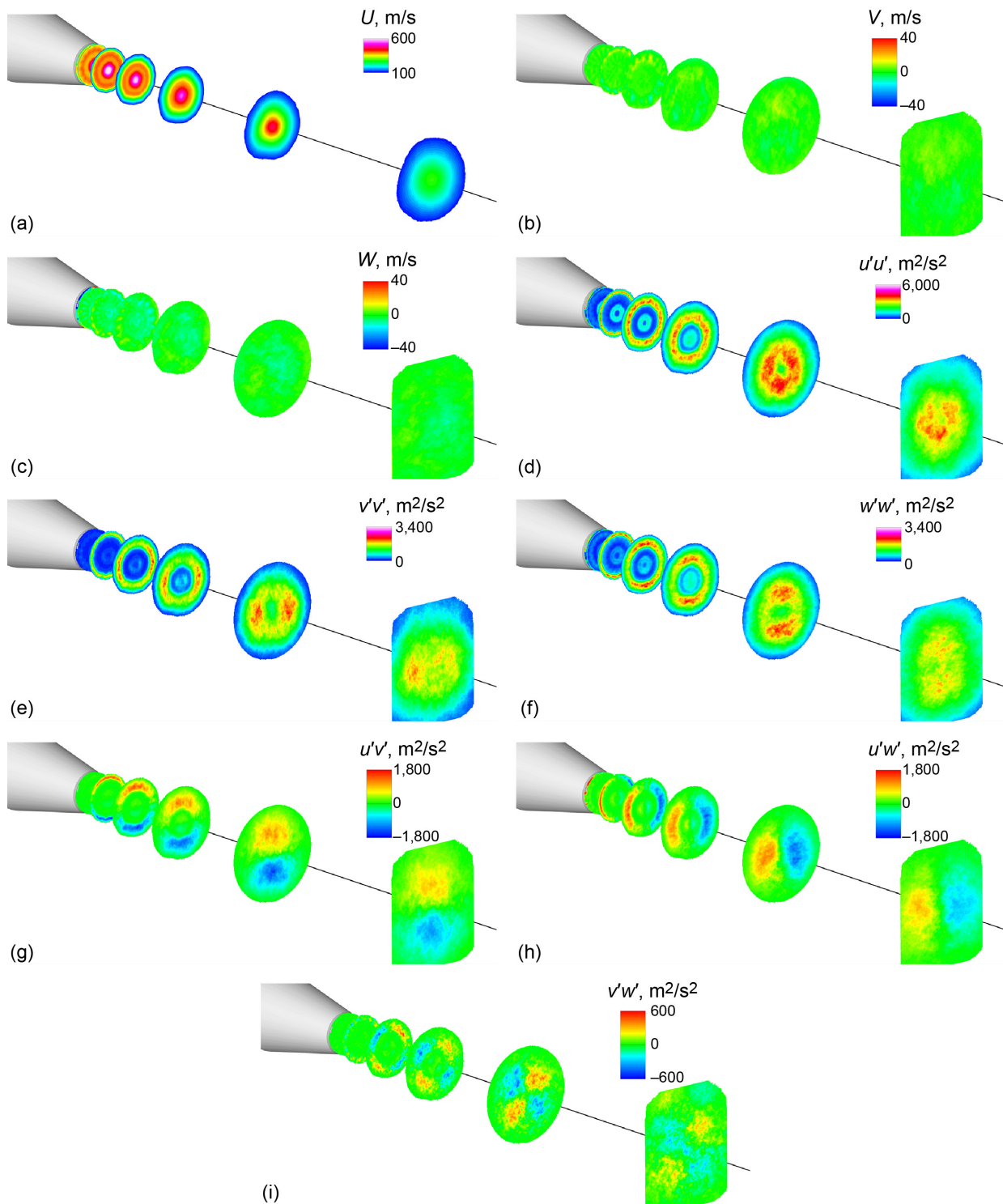


Figure 34.—Turbulent velocity statistics for *Am5plnt*, setpoint 1200, using PIVxa optics. (a) U , m/s. (b) V , m/s. (c) W , m/s. (d) $u'u'$, m^2/s^2 . (e) $v'v'$, m^2/s^2 . (f) $w'w'$, m^2/s^2 . (g) $u'v'$, m^2/s^2 . (h) $u'w'$, m^2/s^2 . (i) $v'w'$, m^2/s^2 .

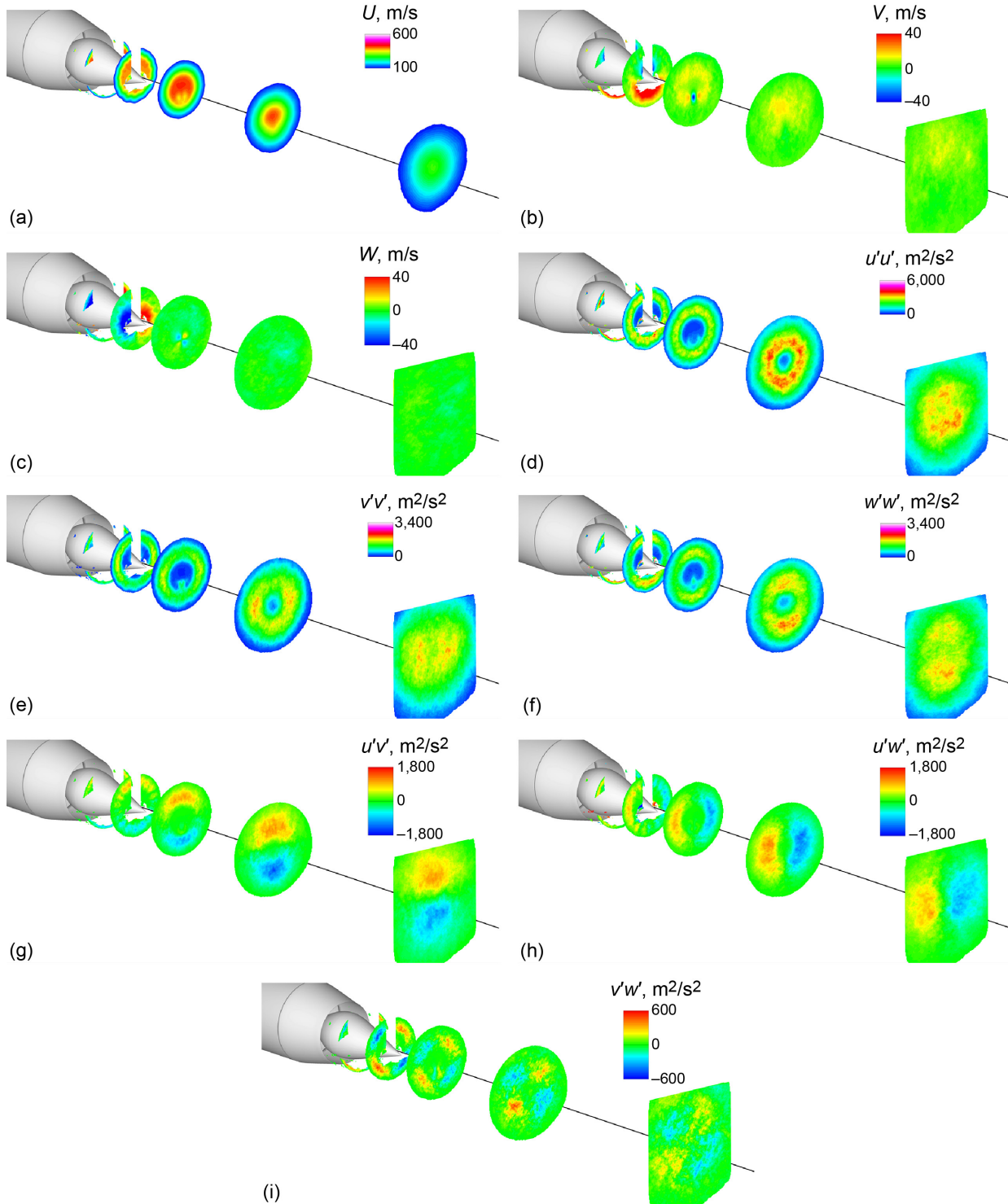


Figure 35.—Turbulent velocity statistics for *DLM5p2069*, setpoint 1200, using PIVxa optics. (a) U , m/s. (b) V , m/s. (c) W , m/s. (d) $u'u'$, m^2/s^2 . (e) $v'v'$, m^2/s^2 . (f) $w'w'$, m^2/s^2 . (g) $u'v'$, m^2/s^2 . (h) $u'w'$, m^2/s^2 . (i) $v'w'$, m^2/s^2 .

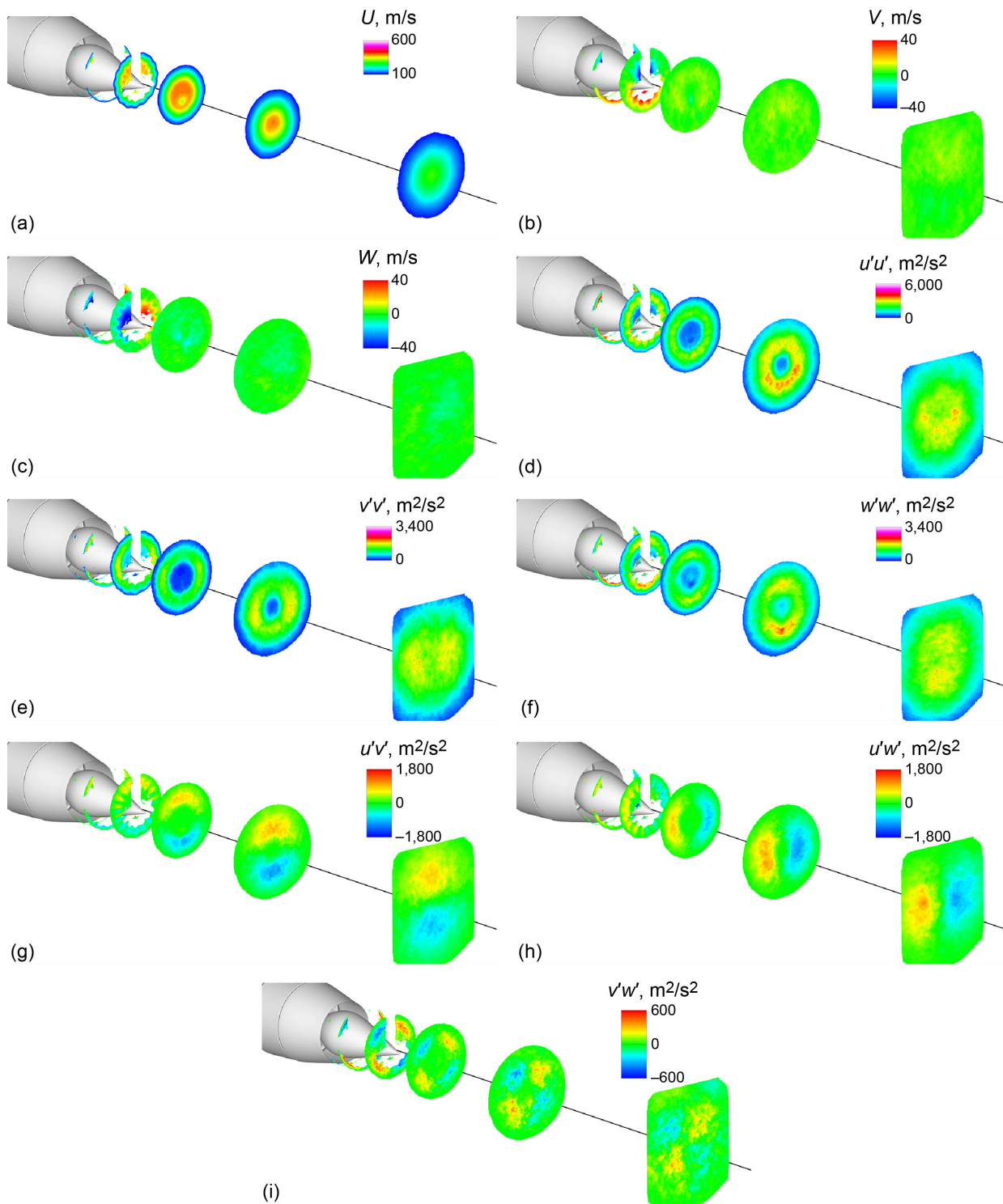


Figure 36.—Turbulent velocity statistics for *DSm5p2069*, setpoint 1200, using PIVxa optics. (a) U , m/s. (b) V , m/s. (c) W , m/s. (d) $u'u'$, m^2/s^2 . (e) $v'v'$, m^2/s^2 . (f) $w'w'$, m^2/s^2 . (g) $u'v'$, m^2/s^2 . (h) $u'w'$, m^2/s^2 . (i) $v'w'$, m^2/s^2 .

The results for the nonstandard stereo cross-stream PIVxb measurements are catalogued in Figure 37 and Figure 38. Recall that the PIVxb optics are set in a coordinate system rotated by 45° from the nozzle

coordinates, which is why in downstream locations the plume cross-sections are truncated at the corners of the y - z space.

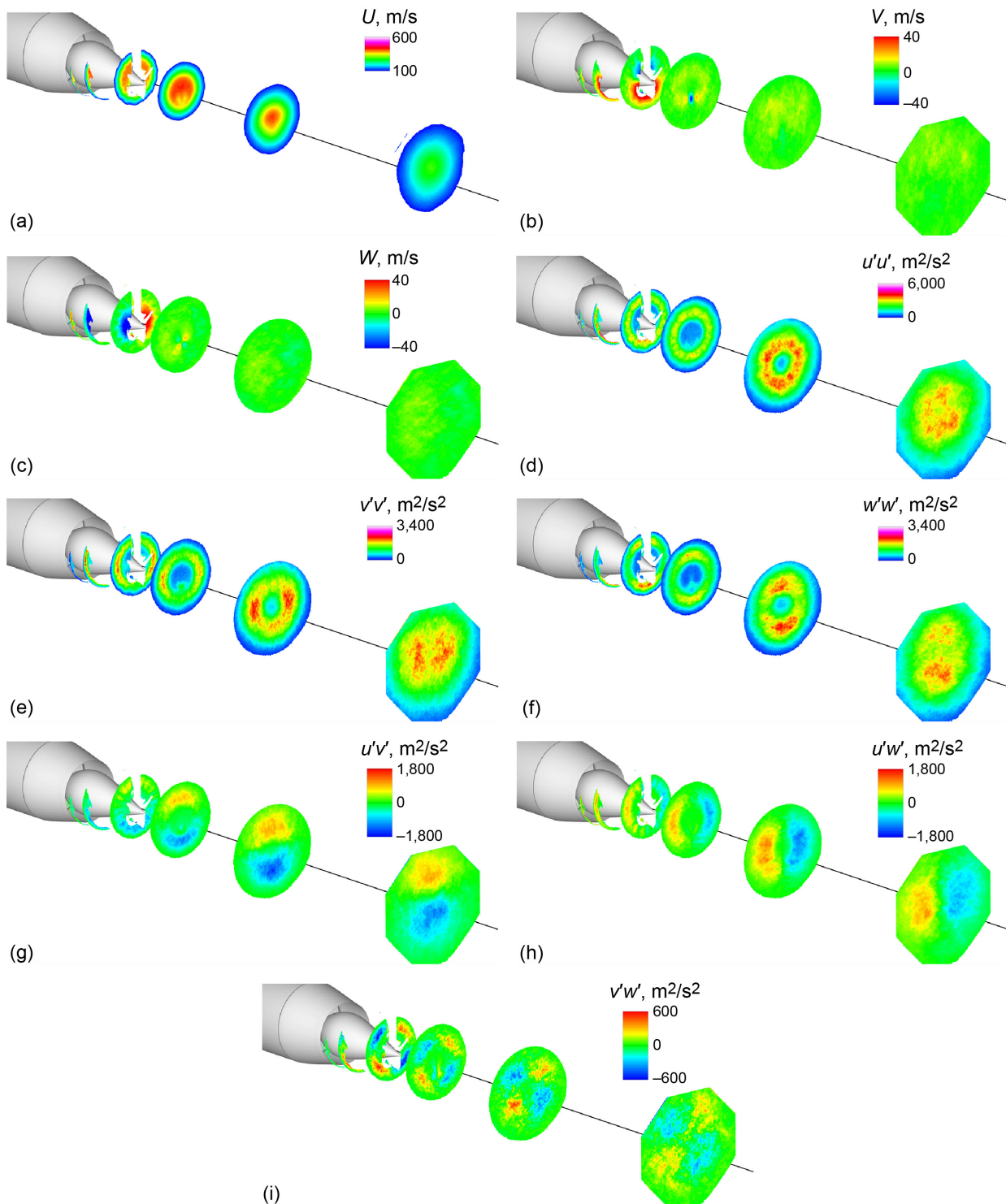


Figure 37.—Turbulent velocity statistics for *DLM5p2069*, setpoint 1200, using PIVxb optics. (a) U , m/s. (b) V , m/s. (c) W , m/s. (d) $u'u'$, m^2/s^2 . (e) $v'v'$, m^2/s^2 . (f) $w'w'$, m^2/s^2 . (g) $u'v'$, m^2/s^2 . (h) $u'w'$, m^2/s^2 . (i) $v'w'$, m^2/s^2 .

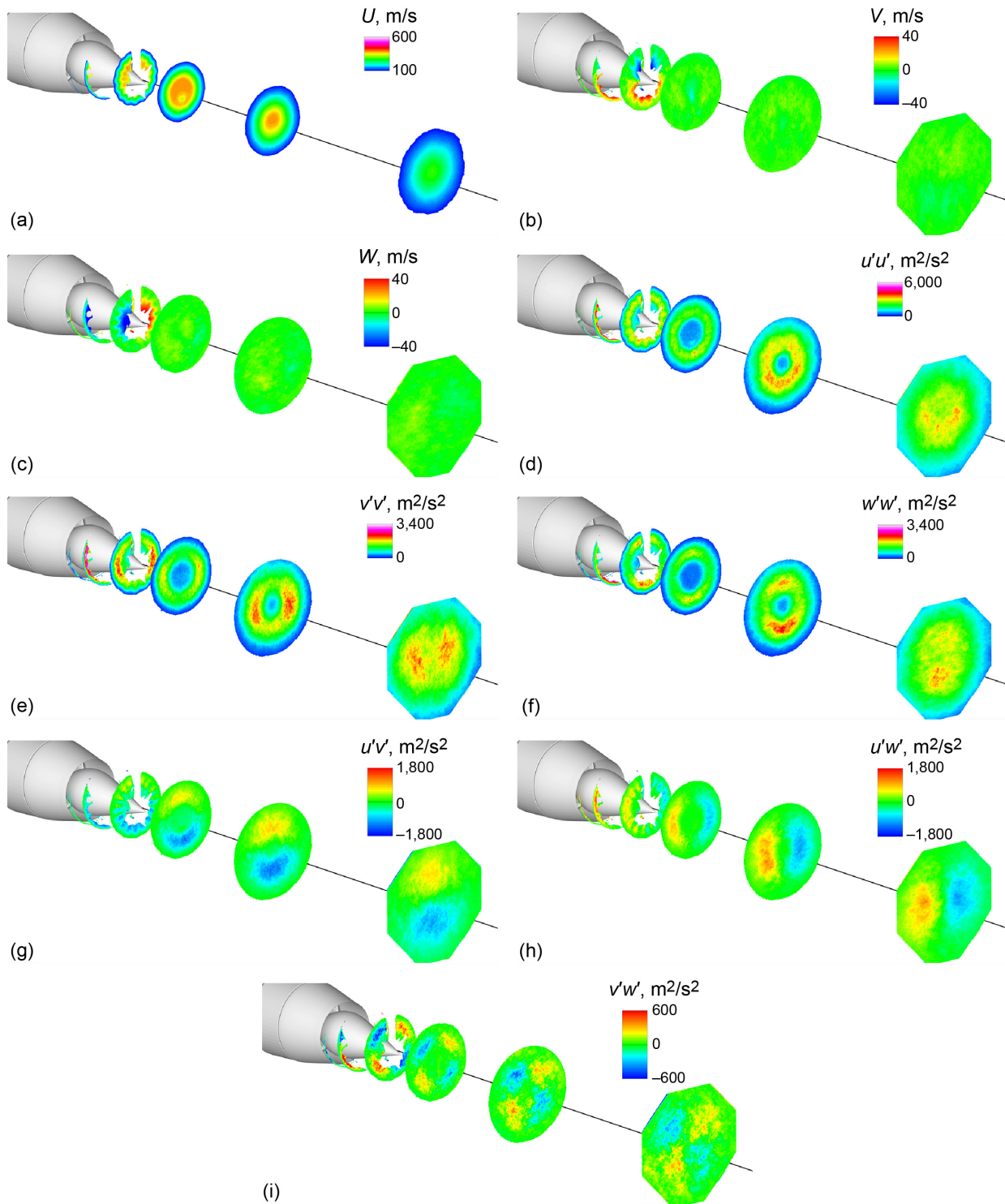


Figure 38.—Turbulent velocity statistics for *DSM5p2069*, setpoint 1200, using PIVxb optics. (a) U , m/s. (b) V , m/s. (c) W , m/s. (d) $u'u'$, m^2/s^2 . (e) $v'v'$, m^2/s^2 . (f) $w'w'$, m^2/s^2 . (g) $u'v'$, m^2/s^2 . (h) $u'w'$, m^2/s^2 . (i) $v'w'$, m^2/s^2 .

When the PIVxa and PIVxb results are directly compared, as seen in Figure 39 and Figure 40, the results agree within the expected uncertainty in regions where they have valid data. On the external plug configuration, neither method yielded very good results for the first two axial stations—the light flare

from the plug produced too many poor vectors to produce quality higher than 70 percent for much of the flow regions of interest. Given that the images for the two measurements were acquired with the same laser pulses, any slight difference comes down to the optical access and to PIV processing, both image and statistics. The image processing (image to displacement) used different software. PIVxa used Wernet's PIVPROC software while PIVxb used DaVis software. In both, several approaches (LogLUT, SPOF, image filtering, etc.) were tried to find the best signal to noise from the images. After this, statistics were computed using different routines to identify and correct instantaneous vector maps based on the statistics of the flow at each spatial point. PIVxa used Chauvenet's criterion with a coefficient of 0.5 to identify and remove outliers. PIVxb used DaVis routines to identify and remove outliers outside four standard deviations in the populations of instantaneous velocities at any given point. This latter should be less restrictive than the Chauvenet's criterion method and may account for some of the differences between PIVxa and PIVxb statistics. The agreement between the two independent methods of processing gives confidence in the accuracy of the measurements.

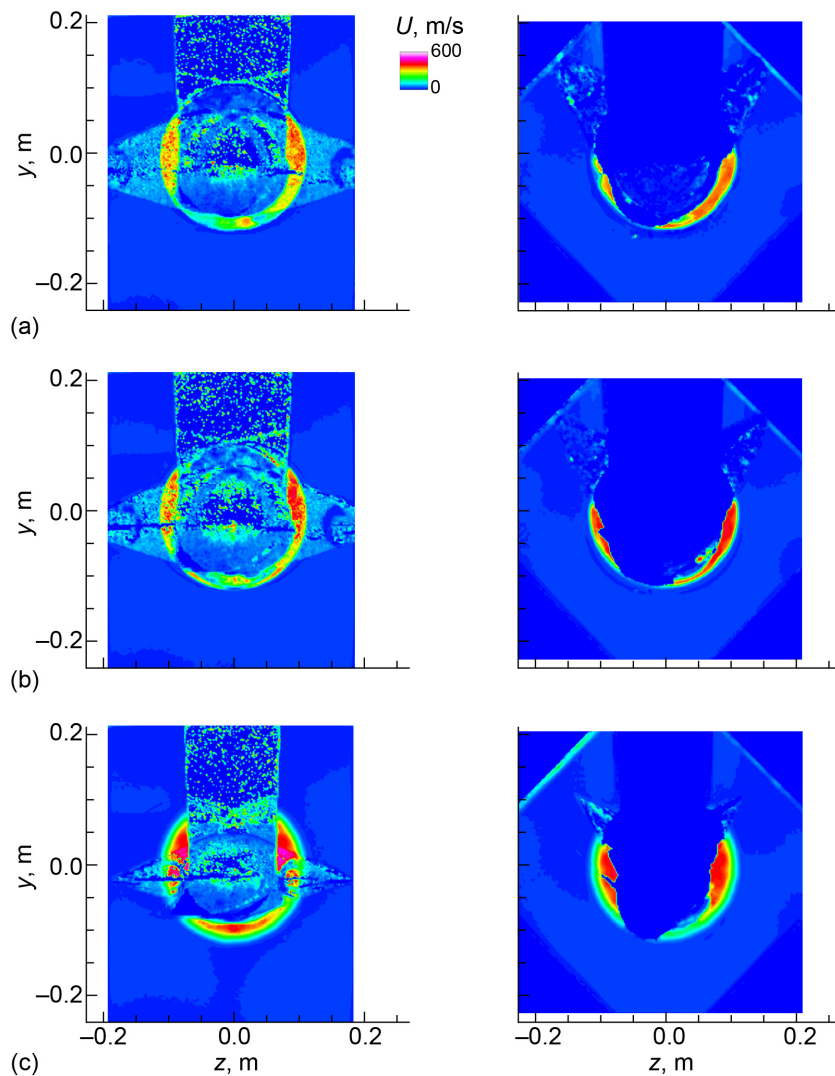


Figure 39.—Average axial velocity, U , as measured by PIVxa and PIVxb. *DLm5p2069*, setpoint 1200. (a) $x = 0.010$ m. (b) $x = 0.025$ m. (c) $x = 0.102$ m. (d) $x = 0.254$ m. (e) $x = 0.508$ m. (f) $x = 1.016$ m. (g) $x = 1.900$ m.

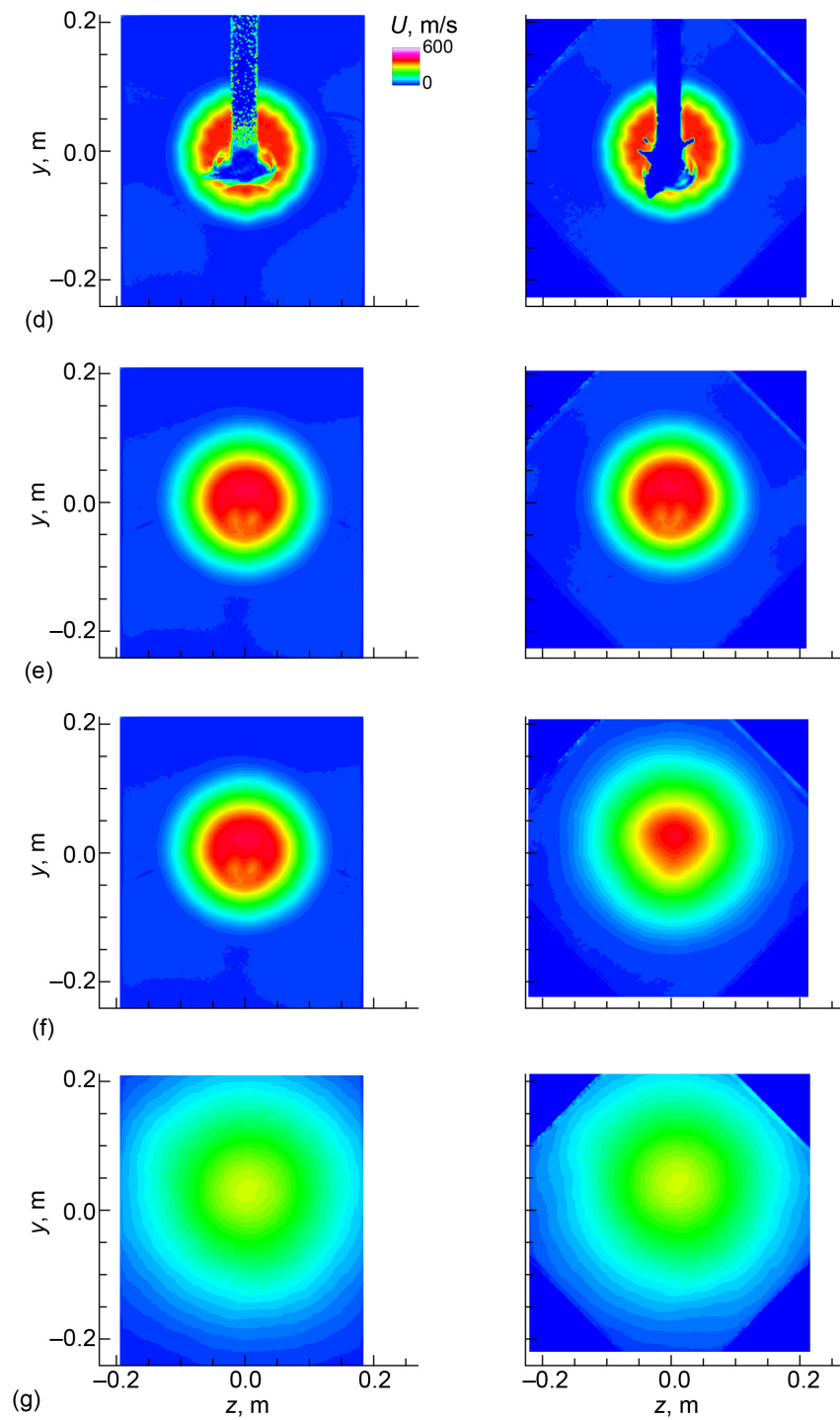


Figure 39.—Concluded.

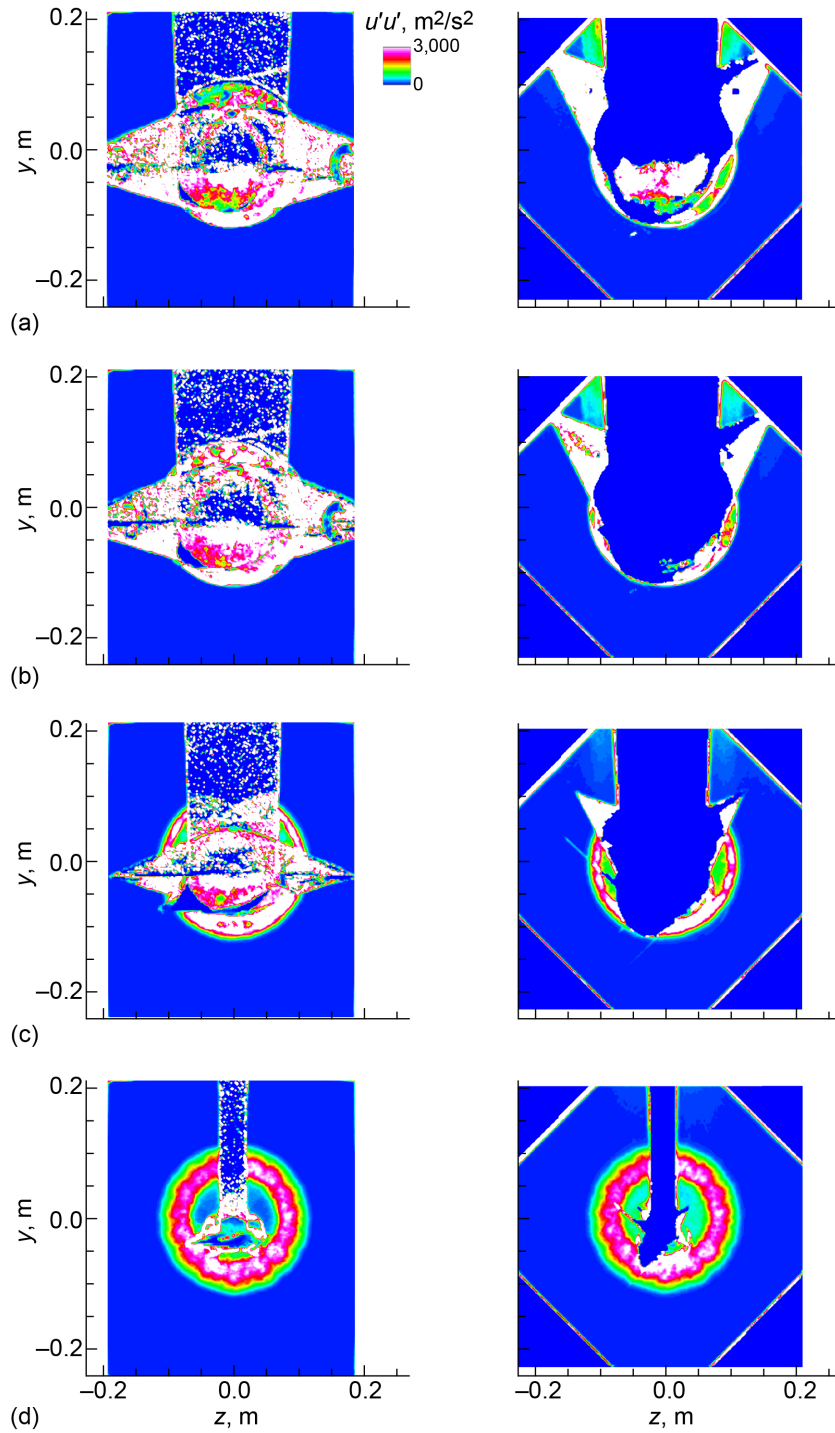


Figure 40.—Variance of axial velocity, $u'u'$, as measured by PIVxa and PIVxb. DLm5p2069, setpoint 1200. (a) $x = 0.010$ m. (b) $x = 0.025$ m. (c) $x = 0.102$ m. (d) $x = 0.254$ m. (e) $x = 0.508$ m. (f) $x = 1.016$ m. (g) $x = 1.900$ m.

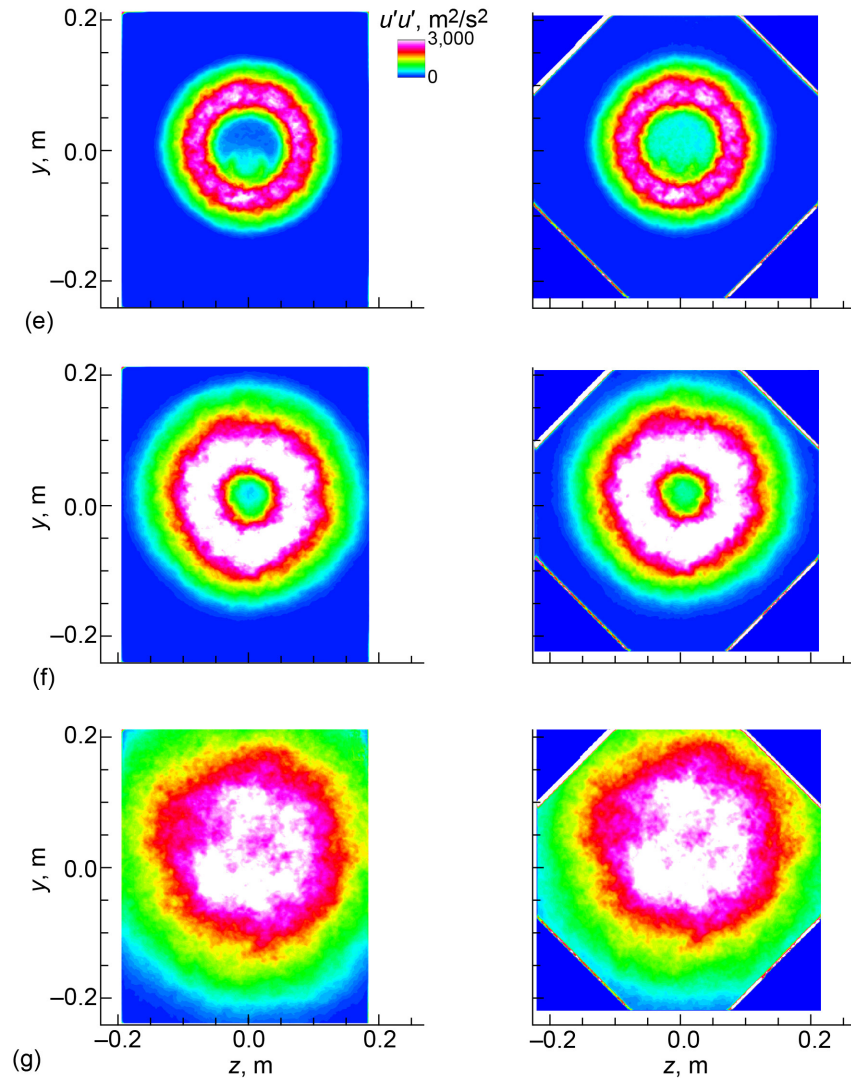


Figure 40.—Concluded.

Another way to look at the accuracy of the cross-stream measurements is to compare them with the streamwise PIVs along the common lines of measurement, i.e., the intersection of the measurement planes. Comparisons of the vertical profiles of mean axial velocity U and the variance of axial velocity $u'u'$ are shown in the plots of Figure 41 (PIVs and PIVxa, *Am0pInt*) and Figure 42 (PIVs and PIVxb, *DLm5p2069*). In these plots, the mean velocities generally agree within 1 to 2 percent. The largest part of the discrepancy is due to the setpoint being defined by ratios of pressure and temperature to ambient, and as the ambient conditions changed between test days, the absolute pressure and temperatures were not quite the same for PIVs and PIVx acquisitions.

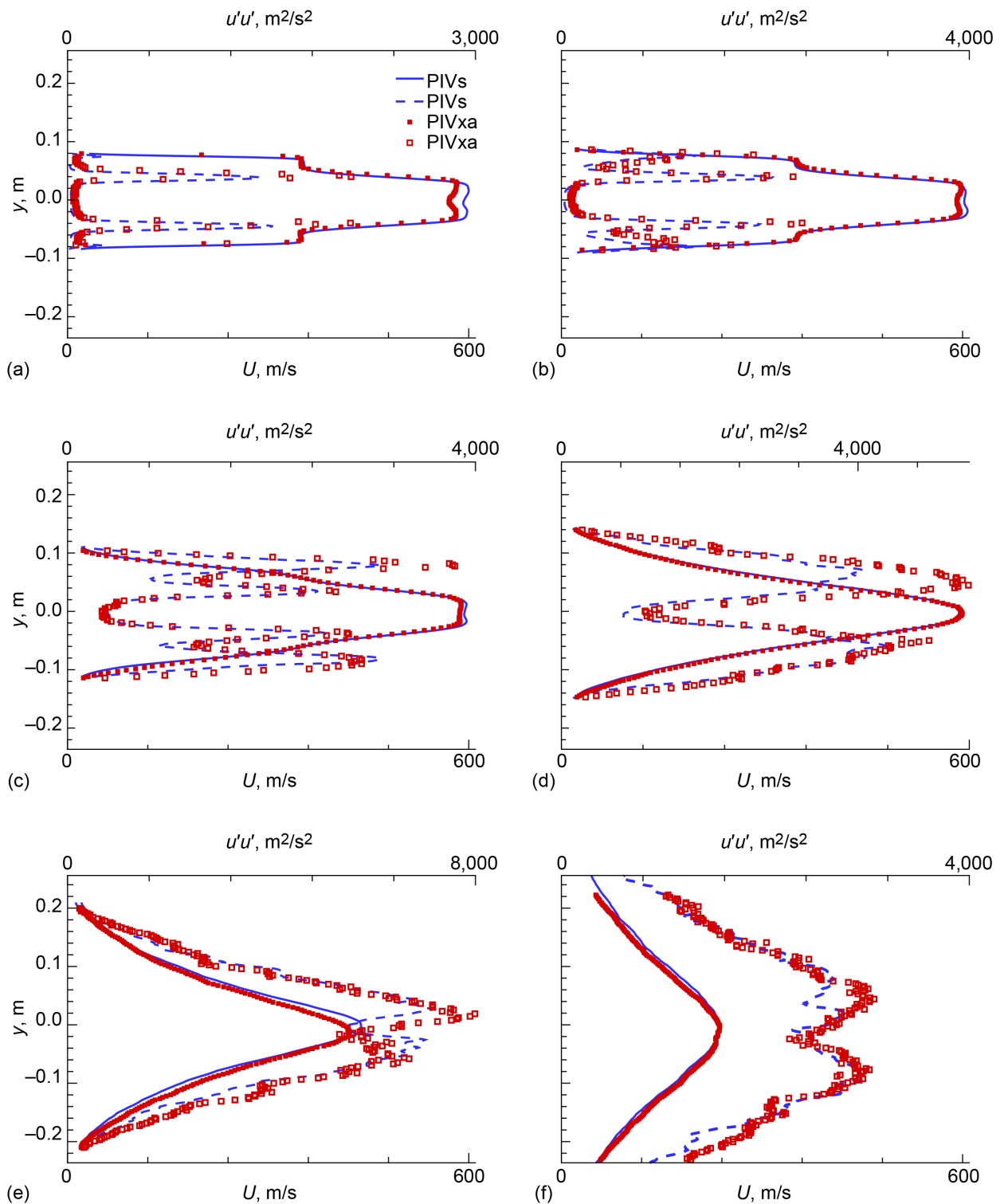


Figure 41.—Comparisons of vertical profiles of mean and variance of axial velocity from PIVs and PIVxa measurements. Axial stations $x = 0.025$ m through 1.906 m, $z = -0.002$ m. *AmOpInt*, setpoint 1200. (a) $x = 0.025$ m. (b) $x = 0.102$ m. (c) $x = 0.254$ m. (d) $x = 0.508$ m. (e) $x = 1.016$ m. (f) $x = 1.906$ m.

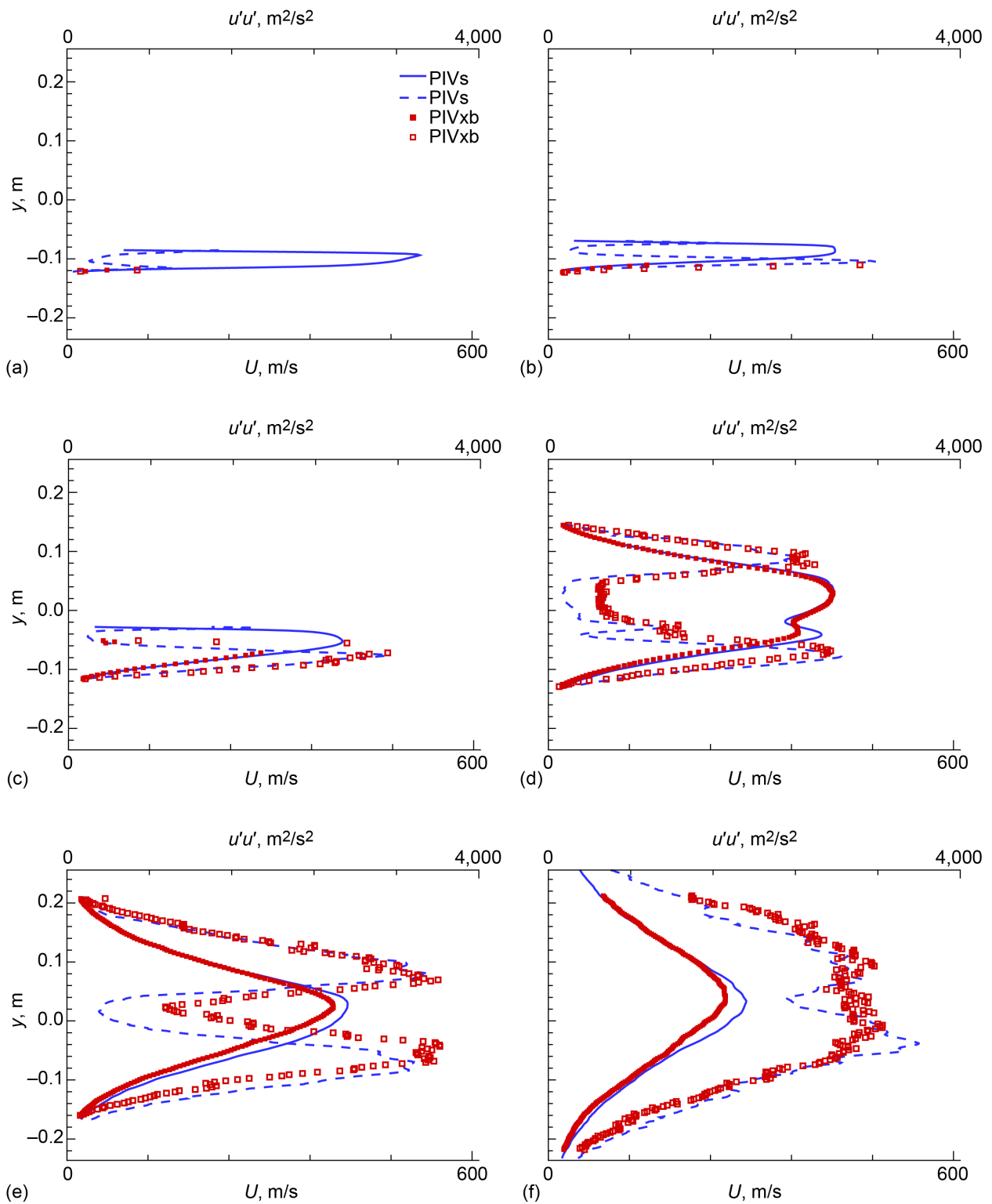


Figure 42.—Comparisons of vertical profiles of mean and variance of axial velocity from PIVs and PIVxb measurements. Axial stations $x = 0.254$ m through 1.9 m, $z = -0.002$ m. *DLM5p2069*, setpoint 1200. (a) $x = 0.025$ m. (b) $x = 0.102$ m. (c) $x = 0.254$ m. (d) $x = 0.508$ m. (e) $x = 1.016$ m. (f) $x = 1.906$ m.

Summary

The Plug20 test program was designed to provide an open dataset of nozzle designs, flow diagnostics, and far-field noise measurements for internally mixed exhaust systems suitable for a commercial supersonic propulsion system operating at takeoff conditions. This report presents the flow diagnostic testing and data for use by developers of flow and noise prediction tools, as well as designers of exhaust nozzle systems. This report also includes hot-shape geometries of the nozzles as tested, which are relevant to users of the far-field noise and other data acquired on this test hardware and reported elsewhere. The mean and turbulent velocities measured using streamwise particle image velocimetry (PIV) are found to be accurate to within a few percent, matching benchmark data established in decades of prior testing. The mean velocities measured in cross-stream planes are also found to be consistent with the streamwise measurements, and thus considered to be accurate. Turbulent quantities measured in the cross-stream plane have inconsistencies and should be used for their spatial pattern rather than their amplitude. The data shown via plots in this report, along with the hot-shape geometries, are in the appendixes.

Appendix A.—CAD Files of Hot Shapes

CAD files of nozzles tested, simplified for flow analysis and modified to reflect the measured geometry at cold and hot flow conditions. Files are in IGES format, one configuration per file. See TM-20230006779SUPPL1.zip for these files.

Appendix B.—Particle Image Velocimetry Data

Velocity statistics of the jet plumes from nozzle configurations are given in Table I, with conditions documented in Table II. The combinations of nozzle and flows acquired are given in Table IV. Two components of velocity, defined in the Results section of the report, were obtained with streamwise PIV and given in the PIVs data files. Three components of velocity were obtained in cross-stream planes and given in PIVx files. The traditional stereo PIV results are denoted as xa; the data obtained with the nonstandard setup are denoted as xb.

File-naming conventions start with the configuration name (e.g., *Dm5p2069*), followed by the setpoint number (e.g., 1200), then one or two letters to denote streamwise (s) or cross-stream (xa or xb), followed by _U1, indicating the single-point statistics. The files are ASCII text, one field point per line. The first line of the file identifies the dataset, defines the variables in each column, and gives the dimensions of the grid. Cross-stream files have each axial plane in a separate block (zone) of data. See TM-20230006779SUPPL2.zip for these supplemental files.

References

1. Mengle, Vinod G.; and Dalton, William N.: Lobed Mixer Design for Noise Suppression: Acoustic and Aerodynamic Test Data Analysis. NASA/CR—2002-210823/VOL1, 2002. <https://ntrs.nasa.gov>
2. Garrison, Loren, et al.: On the Development of Semi-Empirical Noise Models for the Prediction of the Noise From Jets With Forced Mixers. AIAA 2004–2898, 2004.
3. Garrison, Loren, et al.: Computational Fluid Dynamics Analysis of Jets With Internal Forced Mixers. AIAA 2005–2887, 2005.
4. Chase, James D.; Garzon, G. Andres; and Papamoschou, D.: Directivity Effects of Shaped Plumes From Plug Nozzles. AIAA 2013–0008, 2013.
5. Bridges, James E.; Podboy, Gary G.; and Wernet, Mark P.: Plug20 Test Report. NASA/TM-20210010291, 2021. <https://ntrs.nasa.gov>
6. Bridges, James E.; and Wernet, Mark P.: Noise of Internally Mixed Exhaust Systems With External Plug for Supersonic Transport Applications. AIAA 2021–2218, 2021.
7. Ramakrishnan, Kishore, et al.: Evaluation of Low Noise Integration Concepts and Propulsion Technologies for Future Supersonic Civil Transports. NASA/CR—2018-219936, 2018. <https://ntrs.nasa.gov>
8. Wernet, Mark P.; and Hadley, Judith A.: A High Temperature Seeding Technique for Particle Image Velocimetry. Meas. Sci. Technol., vol. 27, no. 12, 2016, p. 125201.

